nature communications

Article

https://doi.org/10.1038/s41467-025-60503-z

# ROMO1 overexpression protects the mitochondrial cysteinome from oxidations in aging

Received: 14 August 2024

Accepted: 23 May 2025

Published online: 03 June 2025

Check for updates

Fengli Xu[1,2,7], Haipeng Huang[1,3,7], Kun Peng[1,2], Chongshu Jian[1], Hao Wu[1], Zhiwen Jing[1], Shan Qiu[1], Ying Chen[4], Keke Liu[5], Ling Fu[5], Yanru Wang[1], Jing Yang[5], Xiaotao Duan[6], Chu Wang[2,4], Heping Cheng[1,2,3] ✉ & Xianhua Wang[1,2,3] ✉

Reactive thiols of proteinaceous cysteines are vital to cell biology by serving as sensor, effector and buffer of environmental redox fluctuations. Being the major source, as well as the prime target, of reactive oxygen species (ROS), mitochondria confront great challenges in preserving their thiol pool. Here we show that ROS modulator 1 (ROMO1), a small inner mitochondrial membrane protein, plays a role in protecting the mitochondrial cysteinome. ROMO1 is redox sensitive and reactive and overexpression can prevent deleterious oxidation of proteinaceous thiols. ROMO1 upregulation leads to a reductive shift of the mitochondrial cysteinome, exerting beneficial effects on mitochondria, such as promoting energy metabolism and $Ca^{2+}$ uniport while inhibiting vicious membrane permeability transition. Importantly, ROMO1 overexpression reverses mitochondrial cysteinome oxidations in multiple organs and slows functional decline in aged male mice. These findings unravel a redox regulatory mechanism of the mitochondrial cysteinome and mark ROMO1 as a potential target for combating oxidative stress and improving healthspan.

Owing to nucleophilicity and redox sensitivity of cysteine thiol[1], proteinaceous cysteine residue is able to both sense and respond to ambient redox changes, constituting a major target for oxidative post-translational modifications. Reversible cysteine oxidations, such as S-sulfenylation, disulfide, or S-glutathionylation, are well-controlled and play a pivotal role in redox regulation by altering protein structure, function and location[2,3]. These oxidative modifications have emerged as a fundamental mechanism in redox signaling of physiological processes such as cell proliferation, differentiation, and migration[4]. In the excess of reactive oxygen species (ROS), however, deleterious oxidations can occur with the reversible thiol oxidations being further irreversibly oxidized to sulfinic acid in most cases and sulfonic acid[5,6]. In addition, the pool of exposed proteinaceous cysteines can serve as a significant buffer to regulate cellular redox homeostasis. It has been shown that the bulk protein thiols are mostly in reductive form under steady state and likely to directly take part in the defense against oxidative stress[7–9]. Hence, the proteinaceous cysteines serve as redox sensor, effector and buffer all at once, and it is critical for cells to maintain a redox sensitive and reactive thiol pool to ensure prompt and proper response upon ambient redox fluctuations. Dysregulation of protein oxidations has been shown to be associated with a plethora of diseases including cardiovascular diseases, neurodegenerative diseases, diabetes, as well as functional decline of organs during aging[4,10,11].

[1]State Key Laboratory of Membrane Biology, Institute of Molecular Medicine, College of Future Technology, Peking University, Beijing, China. [2]Peking-Tsinghua Center for Life Sciences, Peking University, Beijing, China. [3]PKU-Nanjing Institute of Translational Medicine, Nanjing, China. [4]Synthetic and Functional Biomolecules Center, College of Chemistry and Molecular Engineering, Peking University, Beijing, China. [5]National Center for Protein Sciences-Beijing, Beijing Institute of Lifeomics, Beijing, China. [6]State Key Laboratory of Toxicology and Medical Countermeasures, Beijing Institute of Pharmacology and Toxicology, Beijing, China. [7]These authors contributed equally: Fengli Xu, Haipeng Huang. ✉e-mail: chengp@pku.edu.cn; xianhua@pku.edu.cn

The mitochondrion is the primary source of ROS within most mammalian cells[12], and the mitochondrial proteome, which is rich in exposed thiols (60–90 mM)[9], is engulfed in a high ROS microdomain created by its own ROS production. In addition, the alkaline matrix environment (~pH 7.8) promotes thiol oxidation by facilitating ionized thiolate formation[13,14], further stressing the cysteines of mitochondrial proteome toward oxidations. As a result, a number of cysteines on Krebs cycle enzymes and respiration chain complexes suffer deleterious oxidations, that can further cause increased ROS production[15–17].

A tantalizing question arising is how the mitochondrion preserves its thiol pool which is critical for its signaling and functions, while confronting enormous oxidative stresses. To date, multiple ROS-detoxifying enzymes including superoxide dismutase (SOD)1 and SOD2, peroxiredoxins (PRDX) 3 and 5, glutathione peroxidase (GPX) 4, and small non-protein antioxidants (e.g. glutathione), as well as various repair enzymes like thioredoxin (TRX) and glutaredoxin, have been found to be localized in mitochondrial matrix or intermembrane space (IMS) and to regulate redox modifications of mitochondrial proteins either directly or indirectly[14,18]. Given that the inner mitochondrial membrane (IMM) is a hot spot of ROS production while being densely packed with hundreds of different types of functional proteins[19,20], it is of interest to determine whether it also harbors any IMM built-in antioxidant mechanism to protect the mitochondrial proteome against high local ROS attacks, more effectively and preventatively.

ROS modulator 1 (ROMO1) is a small IMM-delimitated, potentially redox-sensitive protein containing 4 cysteines among a total of 79 amino acids. ROMO1 has been reported to increase or decrease ROS production depending on the cell type[21–28]. While these conflicting effects may reflect variations in ROS metabolism across different cell types, they collectively point to a potential role for ROMO1 in redox regulation. It also participates in importing YME1L but is dispensable for general mitochondrial protein import[27] and regulates mitochondrial morphology through affecting OPA1 processing[28].

In the current study, by leveraging the activity-based protein profiling (ABPP) analysis[29,30] to comprehensively profile redox modification changes of the mitochondrial cysteine proteome (mitochondrial cysteinome) in multiple tissues of both young and old mice, we demonstrate that ROMO1 plays an important role in controlling redox homeostasis of the mitochondrial cysteinome. Importantly, with promoting the reductive shift of the mitochondrial cysteinome, ROMO1 exerts beneficial impacts on multiple mitochondrial functions. Further, we show that ROMO1 upregulation counteracts oxidative shift of the mitochondrial cysteinome and retards functional decline in multiple organs of mice during aging.

## Results

### Distinctive molecular properties of ROMO1 in redox sensitivity and reactivity

ROMO1, a small hydrophobic protein comprising 79 amino acids with 4 cysteine residues, is highly conserved across species (Supplementary Fig. 1a) and is ubiquitously expressed in all mouse tissues and organs examined (Supplementary Fig. 1b). Biochemical analysis showed that ROMO1 is predominantly enriched in the IMM subfraction (Supplementary Fig. 1c). In conjunction with APEX2-dependent proximity labeling[31], electron microscopy showed that both its N- and C-termini are facing the IMS (Fig. 1a). Structure prediction using AlphaFold protein structure database[32,33] suggested a topology containing two transmembrane domains (Fig. 1b), thus placing its four cysteines in three sub-compartments: C15 and C79 in close proximity to the outer face of the IMM, C27 within the IMM, and C42 flanking the IMM from the matrix side (Fig. 1b).

The redox sensitivity of cysteines on purified ROMO1 was examined by a mPEG2K-MAL labeling assay. We found that pre-oxidized ROMO1 cysteines were reduced in a graded manner as the reducing potential was increased, evidenced by gradually rising of mPEG2K-MAL-labeled cysteine numbers and abundance (Supplementary Fig. 1d, e). The midpoint redox potentials ($E_m$s) corresponding to reducing one, two, three, and four cysteine residues were estimated to be -271.8 ± 3.8, -302.6 ± 2.3, -354.3 ± 4.4, and -408.8 ± 2.7 mV, respectively (Supplementary Fig. 1f). By comparison, the $E_m$ of $NAD^+$/NADH, the most prominent redox pair for mitochondrial respiration and substrate metabolism, is about -320 mV[34]. This in vitro measurement strongly suggests that purified ROMO1 is intrinsically redox-hypersensitive over a wide range starting at a very low $E_m$, although the exact $E_m$s of ROMO1 in situ would be impacted by its surrounding structural and dielectric environments.

In principle, the redox-hypersensitive cysteines on ROMO1 could intercept and quench ambient ROS. Indeed, purified wild type (WT) ROMO1 dose-dependently removed $H_2O_2$ with a rate constant estimated to be at least $7.5 \times 10^3$ $M^{-1} \cdot s^{-1}$ (Fig. 1c and Supplementary Fig. 1g), while the mutant ROMO1 of which the four cysteines were converted to serine exerted little effect on neutralizing $H_2O_2$ (Fig. 1c). The oxidized ROMO1 can be effectively reduced back by either GSH- or TRX2-reducing system (Fig. 1d, e). We further showed that ROMO1 undergoes reversible oxidation to form disulfide-bonded homodimer after $H_2O_2$ treatment, which is also sensitive to the reduction by GSH- and TRX2-reducing systems (Fig. 1f). These results indicate that purified ROMO1 can detoxify $H_2O_2$ by forming reversible disulfides in vitro. Moreover, we examined the ability of ROMO1 to eliminate $H_2O_2$ in intact mitochondria by measuring mitochondrial aconitase activity, which is particularly susceptible to oxidative damage[35]. The *Romo1* pan-tissue transgenic (TG) (Supplementary Fig. 3a, b) and WT mice were used for mitochondrial isolation. Under basal conditions, both the heart and the liver TG mitochondria showed comparable aconitase activity as those of WT mice (Fig. 1g); however, ROMO1 upregulation in both tissues markedly attenuated the inactivation of aconitase in response to $H_2O_2$ treatment (Fig. 1g).

While determining biochemical reactivity of ROMO1 cysteines in cells with non-reducing SDS-PAGE gel, we found that a substantial proportion of overexpressed ROMO1 was resolved as a series of high molecular weight species (>15 kD), in addition to its monomer form (~12 kD, tagged with 3×FLAG) (Fig. 1h). These high molecular weight species were DTT-sensitive and inducible by $H_2O_2$ treatment (Fig. 1h). We conclude these species are more likely to reflect intermolecular disulfide formation between ROMO1 and interacting proteins rather than ROMO1 oligomers as there was no overt decrease of the ROMO1 monomer following $H_2O_2$ treatment (Fig. 1h). We then performed an in vitro assay by incubating purified ROMO1 with different mitochondrial proteins including succinate dehydrogenase complex (SDH), adenine nucleotide translocator (ANT) 2, and mitochondrial calcium uniporter (MCU) followed by mass spectrometry identification. The results showed that purified ROMO1 formed inter-disulfides with either SDHA or ANT2 or MCU after $H_2O_2$ treatment (Fig. 1i and Supplementary Fig. 2), demonstrating the ability of ROMO1 to form intermolecular disulfides. In this in vitro assay, only ROMO1 C15 was detected to form inter-disulfides with different cysteine sites on the three target proteins, suggestive of its redox hyperreactivity under this experimental condition. Such oxidation-induced intermolecular disulfide formation is sensitive to reduction by both GSH- and TRX2-reducing systems (Fig. 1j).

Since thiol is prone to deleterious and irreversible oxidations to sulfinic acid or sulfonic acid in the presence of excessive ROS[5,6], we speculated that ROMO1 may have dual activity in both scavenging ROS and forming intermolecular disulfides. This prompted us to assess whether ROMO1 can prevent thiol irreversible oxidations. With the aid of a diazene-based alkyne probe[36,37], we detected the extent of thiol sulfinic oxidation and revealed a dramatic increase of thiol sulfinic oxidation by $H_2O_2$ treatment in control cells (Fig. 1k). In contrast,

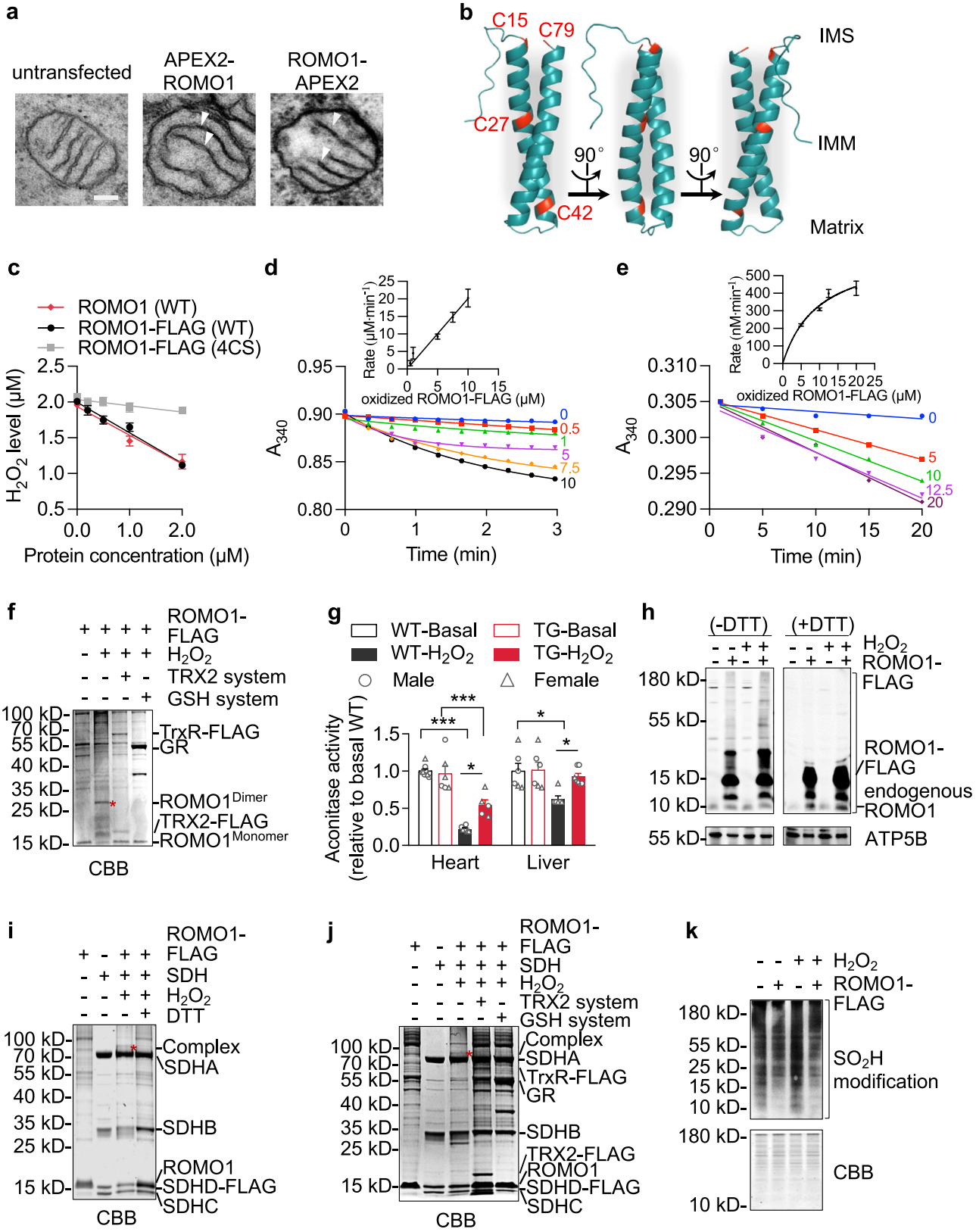


overexpression of ROMO1 almost abolished such ROS-induced irreversible thiol oxidation (Fig. 1k).

Collectively, these results support the conclusion that ROMO1 contains redox sensitive and reactive cysteines which can detoxify ROS in vitro and preemptively form intermolecular disulfides. At this stage, we do not know whether this reflects the activity of ROMO1 in cells.

### Overexpression and conditional knockout of *Romo1* lead to bidirectional redox shifts of the mitochondrial cysteinome

We then hypothesized that ROMO1 might act as a potential redox regulator of the mitochondrial proteome. By implementing ABPP analysis modified as previously reported[19,20] (Supplementary Fig. 4a), we aimed to assess changes of the mitochondrial cysteinome redox landscape in the TG versus WT mice. To this end, the mitochondria

**Fig. 1 | ROMO1 is able to scavenge ROS and form reversible intermolecular disulfides, protecting protein cysteines against irreversible oxidations.** **a** Electron micrographs of mitochondria in HEK293T cells, either untransfected or stably expressing ROMO1-APEX2 or APEX2-ROMO1 fusion proteins. Note that APEX2-related dark staining (white arrowheads) was confined to the inner membrane space (IMS), indicating that both the N- and C-termini of ROMO1 face the IMS. Scale bar, 200 nm. Images are representative of ≥9 fields of view from 3 independent experiments. **b** ROMO1 structure predicted using AlphaFold Protein Structure Database (AF-P60602-F1) and the human gene sequence. The four cysteine residues are highlighted in red. Produced with PyMOL (www.pymol.org). **c** In vitro $H_2O_2$ detoxification assay. Purified human wild type (WT) ROMO1, ROMO1-FLAG, and mutant ROMO1-FLAG in which four cysteines were converted to serine (4CS), were used at concentrations ranging from 0 to 2 μM, with the addition of 2 μM $H_2O_2$. Data are mean ± s.e.m. $n = 7, 4, 5$ measurements from 3 independent experiments for 0 μM, 1 μM, and 2 μM ROMO1 (WT), respectively; $n = 12, 8, 9, 8, 8$ measurements from 3 independent experiments for 0 μM, 0.2 μM, 0.5 μM, 1 μM, and 2 μM ROMO1-FLAG (WT), respectively; $n = 8, 11, 5, 5, 3$ measurements from 3 independent experiments for 0 μM, 0.2 μM, 0.5 μM, 1 μM, and 2 μM ROMO1-FLAG (4CS), respectively. Note that ROMO1 and ROMO1-FLAG show similar $H_2O_2$ detoxifying activity. **d** Kinetic analysis of GSH-reducing system-mediated reduction of pre-oxidized ROMO1-FLAG. The reduction of pre-oxidized ROMO1-FLAG was assessed using a coupled spectrophotometric assay. The inset shows a plot of the initial NADPH consumption rates against different concentrations of pre-oxidized ROMO1-FLAG. A rate constant ($k = 2.0 \times 10^3 M^{-1}s^{-1}$) was determined. Data are mean ± s.d. $n = 3, 3, 5, 3, 3, 3$ measurements from 3 independent experiments for 0 μM, 0.5 μM, 1 μM, 5 μM, 7.5 μM, and 10 μM pre-oxidized ROMO1-FLAG, respectively. **e** Kinetic analysis of TRX2-reducing system-mediated reduction of pre-oxidized ROMO1-FLAG using coupled spectrophotometric assay. The inset shows a plot of initial NADPH rates against different concentrations of pre-oxidized ROMO1-FLAG. Apparent $K_m$ ($K_{m,\ app} = 9.8 \times 10^{-6}$ M) and apparent $V_{max}$ ($V_{max,\ app} = 653\ nM^{-1}min^{-1}$) were determined. Data are mean ± s.d. $n = 3$ measurements from 3 independent experiments for different concentrations of pre-oxidized ROMO1-FLAG. **f** Non-reducing SDS-PAGE analysis for disulfide-bonded homodimer formation of ROMO1 and its sensitivity to TRX2- and GSH-reducing systems. ROMO1-FLAG protein was pre-oxidized with 10 μM $H_2O_2$. The ROMO1-FLAG homodimer is indicated by the red asterisk. GR, glutathione reductase. TrxR, thioredoxin reductase. Coomassie brilliant blue (CBB) R-250 staining was used. **g** Changes of aconitase activity in young WT and TG cardiac or liver mitochondria following $H_2O_2$ treatment. Heart and liver mitochondria were exposed to 50 and 200 μM $H_2O_2$, respectively. Data are mean ± s.e.m. For heart mitochondria, $n = 8$ mice (4 M 4 F) in WT-Basal, $n = 6$ mice (3 M 3 F) in TG-Basal, $n = 6$ mice (3 M 3 F) in WT-$H_2O_2$, $n = 5$ mice (2 M 3 F) in TG-$H_2O_2$; for liver mitochondria, $n = 6$ mice (3 M 3 F) in WT-Basal, $n = 6$ mice (3 M 3 F) in TG-Basal, $n = 6$ mice (3 M 3 F) in WT-$H_2O_2$, $n = 7$ mice (4 M 3 F) in TG-$H_2O_2$. 3-month-old WT and TG mice were used. **h** Anti-ROMO1 western blots showing DTT-sensitive high molecular weight complexes in neonatal rat cardiomyocytes. Note that their formation was promoted by ROMO1-FLAG overexpression and $H_2O_2$ treatment (200 μM). Anti-ATP5B served as the internal control. **i** In vitro intermolecular disulfide formation assay using purified ROMO1-FLAG and SDH complex. SDHA and ROMO1 formed a complex (red asterisk) after 100 μM $H_2O_2$ treatment, which was sensitive to DTT (10 mM). CBB staining was used. **j** Reduction of the intermolecular disulfide between ROMO1 and SDHA by TRX2- and GSH-reducing systems. Red asterisk indicates the ROMO1-SDHA complex. CBB staining was used. **k** Overexpressing ROMO1-FLAG alleviated *S*-sulfinic levels induced by 200 μM $H_2O_2$ treatment in neonatal rat cardiomyocytes. A diazene-based alkyne probe was used to label *S*-sulfinylated proteins. CBB staining served as the internal control. Data in **f, h**–**k** are representative of three independent experiments. In **g,** two-way ANOVA with Tukey's multiple comparisons test was used. $^*p < 0.05$, $^{***}p < 0.001$. Source data are provided as a Source Data file.

were isolated from multiple tissues and organs, including heart, skeletal muscle, liver, and brain for mitochondrial cysteinome redox characterization (Supplementary Fig. 4a). A globally reductive shift in the mitochondrial cysteinome was found in all the four tissues of TG mice (Fig. 2a–e). In particular, 93%, 98%, 98%, and 71% of the redox status-altered cysteines were switched to more reductive states in the heart, skeletal muscle, liver, and brain, respectively (Fig. 2a–e and Supplementary Data 1). Notably, C15 and C42 but not C27 nor C79 of ROMO1 were consistently detected with augmented ABPP labeling (Fig. 2a–d), suggesting that C15 and C42 may serve as the redox-reactive sites under physiological conditions. A technical caveat to this cysteine redox-status profiling is that protein expression could have also contributed to altered cysteine labeling. To discriminate between these two possibilities, we measured protein abundance using LC-MS/MS and found no correlation between the protein abundance and cysteine reactivity changes (Supplementary Fig. 4b), indicating that the cysteine reactivity changes primarily reflect alterations of redox status of the mitochondrial cysteinome.

Next, we determined possible effects of ROMO1 loss-of-function in regulating redox modifications of the mitochondrial cysteinome. Pilot experiment showed that whole-body *Romo1* knockout was embryonically lethal (Supplementary Fig. 3d), suggesting an essential role of ROMO1 in mouse embryonic development. We then generated *Romo1* cardiomyocyte-specific knockout (cKO) and hepatocyte-specific knockout (hKO) mice (Supplementary Fig. 3c, e). In contrast to the reductive shift in the TG mitochondria, we found an oxidative shift of the mitochondrial cysteinome in both cKO heart and hKO liver as compared to their respective control mice (Fig. 2f–h, Supplementary Fig. 4c and Supplementary Data 2). In the cKO heart, 224 sites among 310 redox-altered cysteines displayed oxidative shift, along with lessened ABPP labeling of ROMO1 C15 and C42 (Fig. 2f, h). Likewise, 83% of the redox-altered sites showed oxidation in hKO liver (Fig. 2g, h). Together with the results from TG mice, these data substantiate a role for ROMO1 in controlling the redox status of the mitochondrial cysteinome.

We then defined a ROMO1-protected cysteinome as the cysteines displaying a reductive shift in the TG mitochondria or an oxidative shift in the KO mitochondria. It is important to stress that we do not mean to imply that these cysteines necessarily form disulfide bonds with ROMO1 and the basis for the redox state shift may be indirect. The mitochondrial proteins showing thiol-protection by ROMO1 permeate all four mitochondrial sub-compartments, i.e., matrix, IMM, outer mitochondrial membrane (OMM), and IMS, regardless of tissue types. Further careful examination revealed that the majority of the ROMO1-protected cysteine sites were tissue-specific: a total of 2040 cysteine sites were identified in the four tissues of TG mice, of which 938 sites were unique to only one tissue, 653 sites were present in two tissues, 383 sites in three tissues and only 66 sites in all tissues examined (Supplementary Fig. 4d). Similar tissue-specificity was found in the KO mice (Supplementary Fig. 4d): out of the 402 more oxidized sites, 383 sites were only found in either cKO or hKO mitochondria. These results suggest that the mitochondrial cysteinomes in different tissues are subjected to tissue-specific redox regulation, likely reflecting tissue-specificity of mitochondrial redox metabolism. Gene ontology analysis revealed that the cysteines protected by ROMO1 mapped to core mitochondrial processes including metabolism, translation, structural organization and respiratory complex assembly (Fig. 2i). Notably, most of the mitochondrial ROS-detoxifying enzymes and small molecular antioxidants examined were unaltered in either ROMO1 TG or KO mitochondria (Supplementary Fig. 5), except that TRX2 was increased in the heart and liver of ROMO1 TG mice, SOD1 was upregulated in the heart of cKO mice, and PRDX5 and GPX4 were upregulated in liver of hKO mice (Supplementary Fig. 5a–d). All these results indicate that ROMO1 plays a role in maintaining the reductive state of the mitochondrial cysteinome.

## ROMO1 exerts beneficial effects on multiple mitochondrial functions

Next, we sought to determine the functional relevance of ROMO1-mediated thiol-protection on mitochondrial proteins. Interestingly, the respiratory chain complexes constitute a major category of putative ROMO1 target proteins, with 69 cysteine sites being thiol-protected on 29 subunits of respiratory Complexes I-V

https://doi.org/10.1038/s41467-025-60503-z

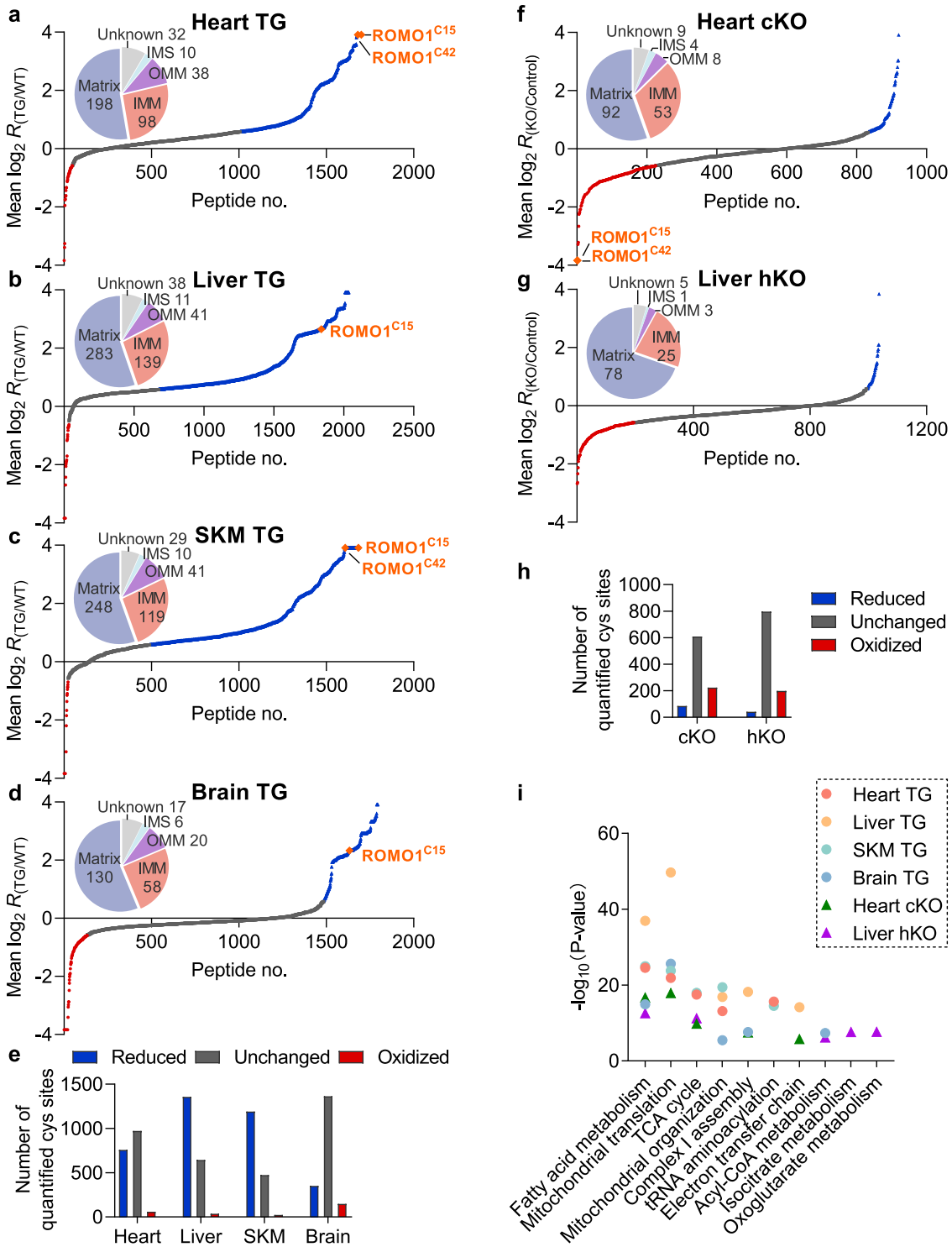


**Fig. 2 | ROMO1 promotes reductive shift of the redox landscape of the mitochondrial cysteinome. a–d** Distributions of the averaged TG/WT activity-based protein profiling ratios of the mitochondrial cysteinome in the heart (**a**), liver (**b**), skeletal muscle (SKM) (**c**), and brain (**d**). Mitochondrial proteome was curated using MitoCarta 3.0. Blue, gray, and red dots indicate reduced ($Log_2R_{(TG/WT)} \geq 0.58$), unchanged ($-0.58 < Log_2R_{(TG/WT)} < 0.58$), and oxidized ($Log_2R_{(TG/WT)} \leq -0.58$) cysteine sites in the TG mitochondria, respectively. Note that C15 and C42 were detected in the four tissues (highlighted). Inset pie charts show sub-mitochondrial distributions of the proteins with reduced cysteine residues. OMM, outer mitochondrial membrane; IMM, inner mitochondrial membrane. $n = 3$-4 independent biological replicates from 6-8 young mice (3-month-old) for each tissue (2 M 4 F for liver; 4 M 4 F for heart, SKM, and brain). **e** Numbers of cysteine sites with or without altered redox status in TG mice as shown in (**a**–**d**). **f, g** As in (**a**–**d**), except that the mitochondrial cysteinome redox changes were measured in the heart of cardiomyocyte-specific *Romo1* knockout (cKO) mice (**f**) or in the liver of hepatocyte-specific *Romo1* knockout (hKO) mice (**g**), along with their respective control groups. $n = 4$ independent biological replicates from 8 mice (4 M 4 F for each group). 3-month-old mice were used. Note that C15 and C42 of ROMO1 were detected in the cKO group. **h** Numbers of cysteine sites with or without altered redox status in KO mice as shown in (**f**, **g**). **i** Gene ontology analysis of the mitochondrial proteins with reduced and oxidized cysteines in the tissues of TG and KO mice, respectively. The top 5 hits in each tissue are shown. Source data are provided as a Source Data file.

(Supplementary Fig. 6a). Functionally, both ATP-coupled and maximal respiratory rates were augmented in TG, but decreased in cKO heart mitochondria (Fig. 3a and Supplementary Fig. 6b, c). Similar results were also found in the primary hepatocytes, i.e., TG cells exhibited enhanced maximal respiratory rate but the opposite result was found in hKO cells (Fig. 3b and Supplementary Fig. 6d, e). Regardless of the rate of mitochondrial respiration, none of the subunits of Complexes I-V examined was affected at the protein level in the heart and liver of either TG or KO mice (Supplementary Fig. 6f, g). These results indicate that ROMO1 upregulation induces thiol reduction of respiratory chain subunits and promotes mitochondrial respiration.

Mitochondrial permeability transition pore (mPTP), also known as a megachannel, is thought to undergo prolonged openings under oxidative stress or $Ca^{2+}$ overload conditions, resulting in mitochondrial swelling and energetic impairment that eventually lead to cell death[38,39]. Although its exact molecular identity is still in debate[40], a number of candidate components or regulators have been identified, including ANT[41,42], cyclophilin D[43–46], and more recently, ATP synthase[47,48]. A substantial number of cysteines on this group of proteins were identified as thiol-protected sites of ROMO1 (Supplementary Fig. 6h, i). We therefore explored possible effects of ROMO1 on $Ca^{2+}$ overload-induced mPTP opening by the assay of mitochondrial $Ca^{2+}$ retention capacity (CRC). The TG mitochondria from heart, or liver, or skeletal muscle all exhibited augmented CRC (Fig. 3c, e and Supplementary Fig. 6j), indicating retardment of mPTP opening. In contrast, both cKO and hKO mitochondria displayed exacerbated mPTP opening reflected by diminished CRC (Fig. 3d, f). In parallel experiments, we assessed the effect of ROMO1 on mPTP opening induced by oxidative stress in cardiomyocytes. Application of 100 μM $H_2O_2$ caused sudden and synchronous loss of mitochondrial membrane potential ($\Delta\Psi_m$) (Fig. 3g, h) and cyclosporin A (CsA) significantly delayed the onset of $\Delta\Psi_m$ loss (Supplementary Fig. 6k). Clearly, ROMO1 upregulation protected the cardiomyocytes against mPTP opening upon oxidative stress, the opposite was found with ROMO1 loss (Fig. 3g, h). Thus, ROMO1 upregulation also confers greater robustness for mitochondria to resist against various stresses.

Further, we investigated the effects of altering ROMO1 expression on mitochondrial $Ca^{2+}$ uptake. Our ABPP labeling revealed that MCU, the core channel portion of the mitochondrial $Ca^{2+}$ uniporter holocomplex[49,50], harbored two ROMO1-protected thiols, C96 and C190, in addition to C65 which was not detected in this assay (Fig. 4a). As compared to WT hearts, the rate of mitochondrial $Ca^{2+}$ uptake was markedly elevated in TG hearts, but decelerated in cKO hearts (Fig. 4b, c, f). Similar bidirectional regulation of mitochondrial $Ca^{2+}$ uniport by ROMO1 was also demonstrated in the liver mitochondria from TG and hKO mice (Fig. 4d–f). These changes may reflect an alteration of MCU activity because neither TG heart nor TG liver nor cKO heart or hKO liver displayed any changes in protein abundance of the uniporter holocomplex subunits, including MCU and MICU1 (Supplementary Fig. 7a, b). We speculate that ROMO1 may promote mitochondrial $Ca^{2+}$ uptake in association with the reduction of MCU C96 and C190.

## Indispensable role of C15 and C42 for ROMO1-mediated thiol protection

Further, we delineated which cysteine or cysteines of ROMO1 are functionally required for its role in thiol-protection by generating ROMO1 mutants with one of the four cysteines converted to serine. We first found that $H_2O_2$-induced formation of disulfide-bonded homodimer was abolished in either purified C15S or C42S ROMO1 mutant, however, C27S and C79S mutants exhibited comparable homodimer formation with WT ROMO1 (Fig. 5a). Consistent with this, C15S or C42S mutation rendered it ineffective in promoting the formation of DTT-sensitive inter-disulfides, whereas C27S or C79S mutation only showed mild effect (Fig. 5b). Further, as compared to WT ROMO1, C27S or C79S mutant remained equally effective in preventing ROS-induced thiol sulfinic oxidation, whereas either C15S or C42S mutation largely blunted this anti-sulfinylation effect (Fig. 5c). To more stringently test the requirement of C15 or C42 for ROMO1 in thiol-protection of the mitochondrial cysteinome, we generated cardiomyocyte-specific C15S or C42S knockin (cKI) mouse models (Supplementary Fig. 7c), which showed comparable expression level of mutant ROMO1 as WT ROMO1 in the control heart (Fig. 5d). Both the C15S and C42S cKI hearts displayed a dramatic oxidation shift of the mitochondrial cysteinome evidenced by robust amelioration of iodoacetamide (IA)-alkyne labeling for reductive thiols (Fig. 5d).

Functionally, we showed that C15 and C42 appeared to be obligatory, while C27 and C79 being dispensable, for ROMO1 inhibition of oxidative stress-induced mPTP opening (Fig. 5e) and subsequent cell death indicated by lactate dehydrogenase release (Fig. 5f). In addition, the requirement for C15 and C42 was substantiated by the different impacts of ROMO1 mutants on mitochondrial $Ca^{2+}$ uptake: C27S or C79S mutant increased mitochondrial $Ca^{2+}$ uptake to an extent comparable to that by WT ROMO1, but either C15S or C42S mutant failed to augment mitochondrial $Ca^{2+}$ uptake (Fig. 5g, h). Similar cytosolic $Ca^{2+}$ transients were detected in all groups upon histamine stimulation, irrespective expression of ROMO1 and its mutants (Supplementary Fig. 7d). Thus, C15 and C42 are functionally essential sites for ROMO1 to play its thiol-protective role in mitochondria.

## ROMO1 upregulation reverses oxidative shift of the mitochondrial cysteinome and retards functional decline during aging

It has been shown that mitochondrial functions progressively deteriorate in association with increased ROS production and impaired ROS detoxification in aging[51,52]. However, the aging-associated alterations of mitochondrial proteomic redox landscape remain unclear. By exploiting the ABPP analysis to profile redox changes of the mitochondrial cysteinome, we revealed a prominent and consistent oxidative shift in multiple organs and tissues (heart, skeletal muscle, liver and brain) in old mice (25 months old) comparing to young mice (3 months old) (Fig. 6a–d, Supplementary Fig. 8a and Supplementary Data 3). Specifically, 65%, 69%, 76%, and 87% of the redox-altered cysteine sites were switched to more oxidized states in the old heart, skeletal muscle, liver and brain, respectively (Fig. 6a–d). In line with oxidative shift of the mitochondrial cysteinome, the protein level of ROMO1 was largely decreased in all the old tissues of WT mice (Supplementary Fig. 10a, b). By measuring mitochondrial aconitase activity, we showed that ROMO1 overexpression not only significantly diminished $H_2O_2$-induced inactivation of aconitase but also enhanced aconitase activity under basal condition in the aged mice (Supplementary Fig. 10c). One possible explanation for this is the idea that ROMO1 contributes to detoxification of aging-associated ROS. ROMO1 upregulation effectively prevented such an oxidative shift of the mitochondrial cysteinome during aging irrespective of organs and tissues involved (Fig. 6e–h, Supplementary Fig. 8b and Supplementary Data 3). The vast majority of the oxidized cysteines in old WT mice, i.e., 89% in the heart, 87% in the skeletal muscle, 86% in the liver and 81% in the brain, were reversed to a more reductive state in the old TG mice (Fig. 6i–l). Moreover, a big part of the ROMO1-protected thiols in the old TG mice were reverted to a similar or even more reductive state compared with those in young WT mice (Supplementary Fig 8c-f). Once again, the aging-associated oxidation landscape of the mitochondrial cysteinome appeared to be highly tissue-specific (Supplementary Fig 8g), suggestive of tissue-specificity of mitochondrial functional changes during aging process. More interestingly, among those that were

https://doi.org/10.1038/s41467-025-60503-z

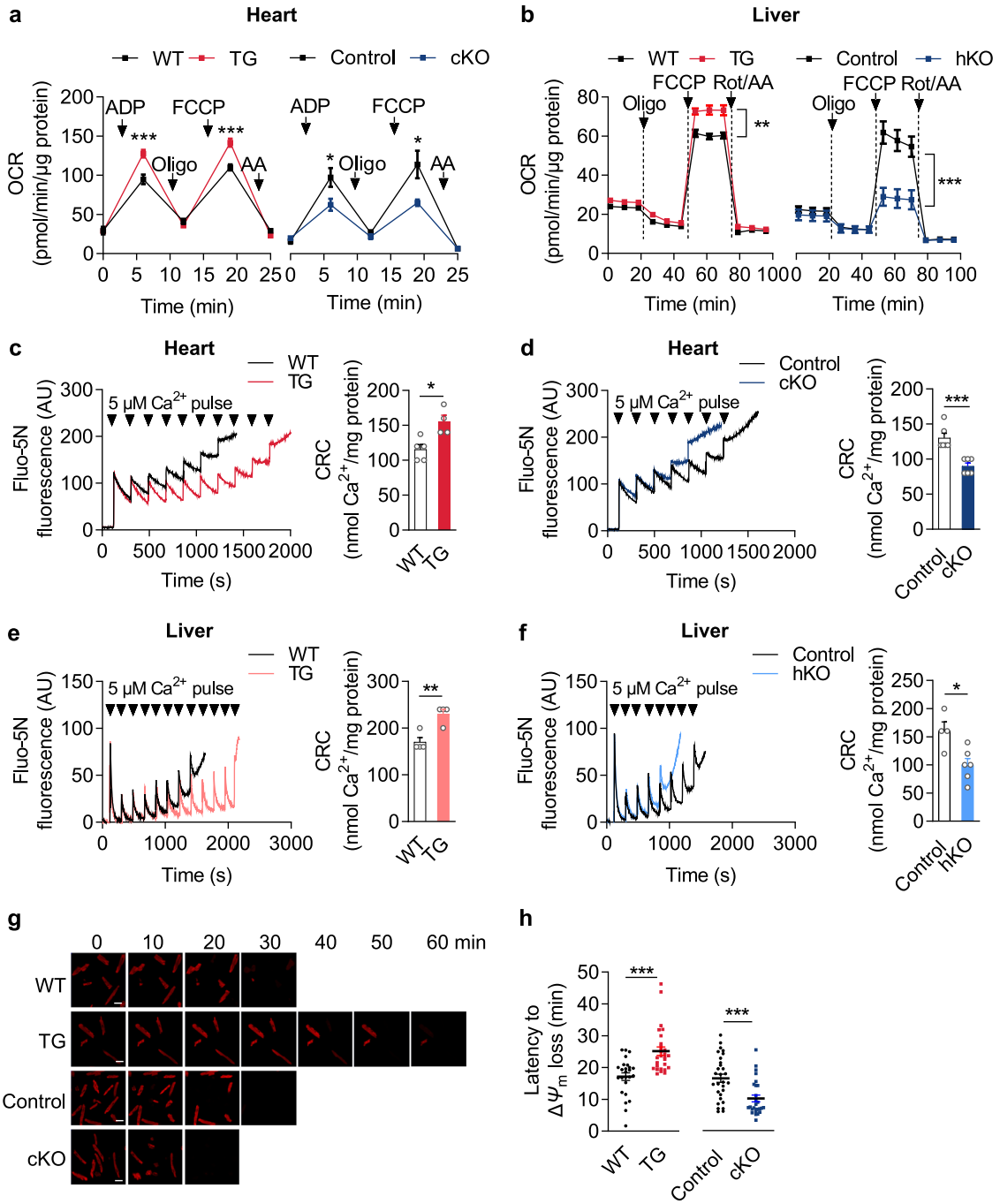


**Fig. 3 | Upregulation and ablation of ROMO1 bidirectionally regulate mitochondrial respiration and mPTP opening. a** Altered oxygen consumption rate (OCR) of heart mitochondria from TG and cKO mice. Glutamate and malate were used as substrates. 250 μM ADP, 4 μM oligomycin (Oligo), 4 μM FCCP, and 2 μM antimycin A (AA) were added sequentially as indicated by the arrows. Data are mean ± s.e.m. $n = 11$ measurements from 3 WT mice, $n = 17$ measurements from 3 TG mice, $n = 9$ measurements from 3 Control mice, $n = 5$ measurements from 3 cKO mice. 3-month-old male mice were used. min, minute. **b** OCR changes of hepatocytes from TG and hKO mice. Glucose and pyruvate were used as substrates. 1 μM Oligo, 1 μM FCCP, and 1 μM rotenone (Rot)/AA were added sequentially as indicated by the arrows. Data are mean ± s.e.m. $n = 4$ measurements from 3 WT mice, $n = 4$ measurements from 3 TG mice, $n = 9$ measurements from 3 Control mice, $n = 9$ measurements from 3 hKO mice. 3-month-old male mice were used. **c**–**f** Opposite effects of ROMO1 upregulation and ablation on $Ca^{2+}$ retention capacity (CRC) of heart and liver mitochondria. Left panels: Representative traces of the CRC assay as indicated by Fluo-5N fluorescence changes. Right panels: Quantifications of mitochondrial CRC. Data are mean ± s.e.m. In (**c**), $n = 5$ WT mice, $n = 4$ TG mice; in (**d**), $n = 6$ Control mice, $n = 6$ cKO mice; in (**e**), $n = 4$ WT mice, $n = 4$ TG mice; in (**f**), $n = 4$ Control mice, $n = 6$ hKO mice. 3-month-old male mice were used. AU, arbitrary units. s, second. **g** Representative confocal images of TMRM fluorescence in isolated mouse cardiomyocytes after 100 μM $H_2O_2$ treatment. mPTP opening was indicated by an irreversible loss of TMRM-reported $\Delta\Psi_m$. Scale bars, 50 μm. **h** Quantifications of latency of mPTP opening indicated by $\Delta\Psi_m$ loss in response to $H_2O_2$ treatment in TG and cKO cardiomyocytes. Data are mean ± s.e.m. $n = 25$ dishes from 4 WT mice, $n = 28$ dishes from 4 TG mice, $n = 29$ dishes from 3 Control mice, $n = 27$ dishes from 5 cKO mice. 3-month-old male mice were used. In **a**–**f, h,** two-tailed unpaired Student's *t*-test with Welch's correction was used. $^*p < 0.05$, $^{**}p < 0.01$, $^{***}p < 0.001$. Source data are provided as a Source Data file.

https://doi.org/10.1038/s41467-025-60503-z

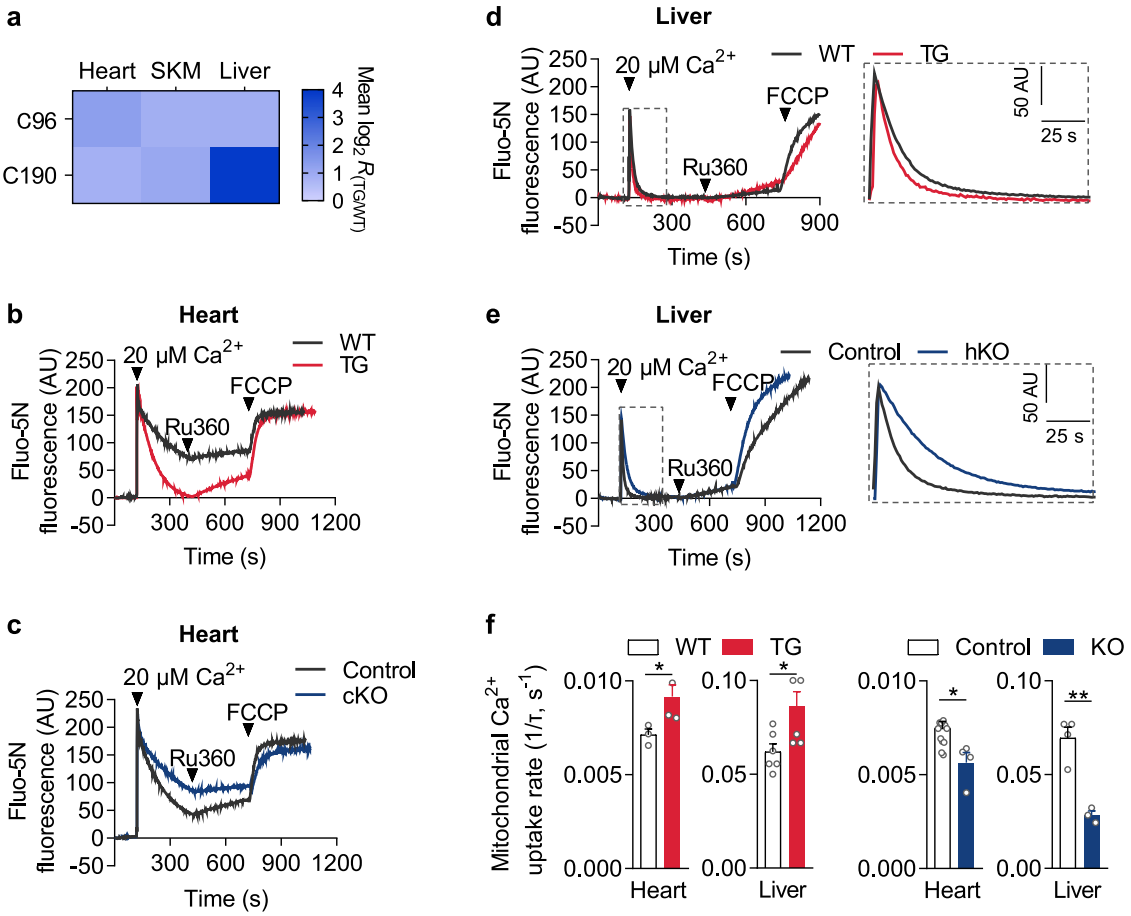


**Fig. 4 | Opposite effects of ROMO1 upregulation and ablation on mitochondrial $Ca^{2+}$ uptake. a** Heat map of the activity-based protein profiling ratios of TG/WT at MCU C96 and C190 in different mouse tissues. $n = 3$-4 independent biological replicates from 6-8 young mice (3-month-old) for each tissue (2 M 4 F for liver; 4 M 4 F for heart and skeletal muscle (SKM)). Darker blue indicates a more reduced state of the cysteine sites in TG compared to WT. **b**–**e** Representative traces of mitochondrial $Ca^{2+}$ uptake responding to 20 μM $Ca^{2+}$ in heart or liver mitochondria isolated from TG or cKO or hKO mice and their respective control mice. Ru360, MCU inhibitor; FCCP, uncoupler of oxidative phosphorylation. In **d** and **e**, enlarged view of the boxed regions are shown to the right. AU, arbitrary units. s, second. **f** Averaged data of mitochondrial $Ca^{2+}$ uptake rate (1/τ, where τ is the respective time constant of extra-mitochondrial $Ca^{2+}$ decay). Data are mean ± s.e.m. For heart mitochondria, $n = 3$ measurements from 3 WT mice, $n = 4$ measurements from 3 TG mice, $n = 12$ measurements from 5 Control mice, $n = 4$ measurements from 4 cKO mice; for liver mitochondria, $n = 6$ measurements from 3 WT mice, $n = 6$ measurements from 3 TG mice, $n = 4$ measurements from 4 Control mice, $n = 3$ measurements from 3 hKO mice. 3-month-old male mice were used. In **f**, two-tailed unpaired Student's *t*-test with Welch's correction was used. $^{*}p < 0.05$, $^{**}p < 0.01$. Source data are provided as a Source Data file.

selectively oxidized in old mice and reductively protected by ROMO1, we applied disease network analysis and identified multiple protein drivers of a series of aging-associated diseases in a particular organ (Supplementary Fig. 9). For example, the drivers of heart failure in the heart (Supplementary Fig. 9b), of myopathy in the skeletal muscle (Supplementary Fig. 9d), of steatohepatitis in the liver (Supplementary Fig. 9f), and of neurodegenerative disorders in the brain (Supplementary Fig. 9h) were coordinately oxidized in old mice, but ROMO1 upregulation effectively protected them from such aging-associated oxidations. These results suggest that ROMO1 counteracts oxidations of the mitochondrial cysteinome in aging, particularly the subgroups of protein drivers underlying aging-related pathologies in specific organs.

In light of this finding, we further examined functional impacts of ROMO1-mediated thiol-protection in aging. In the heart, ROMO1 upregulation reversed the age-associated decline of cardiac contractile function indexed by ejection fraction and fractional shortening (Fig. 7a, b), with no sign of cardiac hypertrophy at old versus young age groups in either WT or TG mice (Supplementary Fig. 10d). In the skeletal muscle, the grip strength decline and muscle atrophy, which are hallmarks of skeletal muscle aging[53], occurred in WT mice, but were greatly attenuated in the TG mice (Fig. 7c–e and Supplementary Fig. 10e). The liver damage markers, including elevated levels of serum aspartate aminotransferase (AST), alanine aminotransferase (ALT) and low density lipoprotein (LDL) were evident in old WT mice, but all were largely repressed in old TG mice (Fig. 7f–h). The serum cholesterol showed a trend of decrease in the old TG mice (Fig. 7i) and other parameters examined, including ratios of liver weight to body weight, serum high density lipoprotein (HDL), blood glucose and serum triglycerides, displayed no significant changes between WT and TG mice at both young and old ages (Supplementary Fig. 10f–i). Ameliorated aging-associated inflammation in the old TG mice was also evidenced by decreased numbers of blood monocytes (Fig. 7j) and neutrophils (Fig. 7k) and lower level of circulating interleukin-6 (Fig. 7l). All these results indicate that ROMO1 upregulation markedly retards function declines of multiple organs during aging in association with reversing organ-specific mitochondrial cysteinome oxidations.

## Discussion

In this study, we leveraged on ABPP analysis of enriched mitochondria to comprehensively profile redox modifications of the mitochondrial cysteinome in multiple mouse tissues (heart, skeletal muscle, liver, and

https://doi.org/10.1038/s41467-025-60503-z

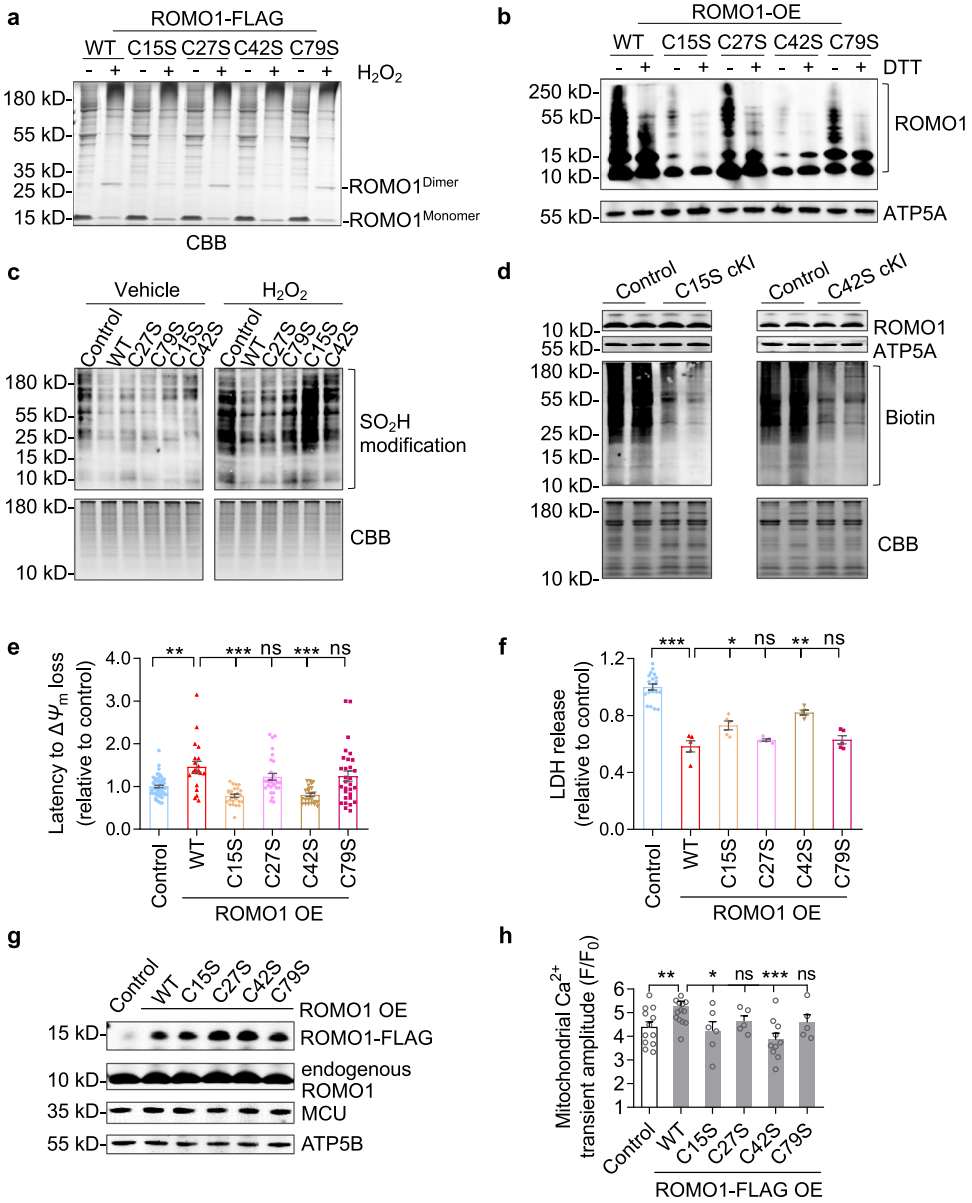


**Fig. 5 | C15 and C42 are functionally essential for ROMO1-mediated thiol-protection. a** Non-reducing SDS-PAGE analysis for disulfide-bonded homodimer formation of WT and mutant ROMO1. Purified human WT or mutant ROMO1-FLAG protein was oxidized with 10 μM $H_2O_2$. CBB staining was used. **b** Anti-ROMO1 western blots showing formation of DTT-sensitive high molecular weight complexes in neonatal rat cardiomyocytes overexpressing WT or C15S, C27S, C42S, or C79S mutant ROMO1. Anti-ATP5A served as the internal control. **c** *S*-sulfinic oxidation levels induced by 200 μM $H_2O_2$ treatment in neonatal rat cardiomyocytes overexpressing WT, or C15S, C27S, C42S, or C79S mutant ROMO1. CBB staining served as the internal control. **d** Iodoacetamide-alkyne labeling showing elevated oxidation of the mitochondrial cysteinome in the C15S or C42S conditional knockin hearts (C15S cKI or C42S cKI). The reactive thiols of the mitochondrial cysteinome were labeled with iodoacetamide-alkyne and then reacted with azide-biotin tag via click chemistry. CBB staining served as the internal control. **e, f** Effects of WT or mutant ROMO1 overexpression (OE) on protecting against oxidative stress (1 mM $H_2O_2$ treatment) induced mPTP opening (**e**) and cell death (**f**) in adult rat cardiomyocytes. mPTP opening was indicated by $\Delta\Psi_m$ loss and cell death was assessed by lactate dehydrogenase (LDH) release. Data are mean ± s.e.m. In **e**, $n = 59$ dishes from 5 independent experiments for Control, $n = 20$ dishes from 5 independent experiments for WT OE, $n = 25$ dishes from 5 independent experiments for C15S OE, $n = 30$ dishes from 5 independent experiments for C27S OE, $n = 24$ dishes from 5 independent experiments for C42S OE, $n = 30$ dishes from 5 independent experiments for C79S OE. In **f**, $n = 20$ measurements from 5 independent experiments for Control, $n = 5$ measurements from 5 independent experiments for WT, C15S, C27S, C42S, and C79S OE. **g** Representative western blots showing comparable expression of WT and C15S, C27S, C42S, or C79S mutant ROMO1-FLAG in HeLa cells. Anti-ATP5B served as the internal control. **h** Effects of overexpressing WT or mutant ROMO1 on mitochondrial $Ca^{2+}$ uptake induced by 100 μM histamine stimulation in HeLa cells. Data are mean ± s.e.m. $n = 12$ dishes from 3 independent experiments for Control, $n = 15$ dishes from 3 independent experiments for WT OE, $n = 6$ dishes from 3 independent experiments for C15S OE, $n = 5$ dishes from 3 independent experiments for C27S OE, $n = 10$ dishes from 3 independent experiments for C42S OE, $n = 5$ dishes from 3 independent experiments for C79S OE. Data in **a**–**d, g** are representative of three independent experiments. In **e, f, h**, two-tailed unpaired Student's *t*-test with Welch's correction was used. $^*p < 0.05$, $^{**}p < 0.01$, $^{***}p < 0.001$; ns, no significance. Source data are provided as a Source Data file.

brain). Using the TG and tissue-specific KO mouse models, we demonstrated that the IMM small protein ROMO1 plays a role in controlling redox status of the mitochondrial cysteinome, exerting beneficial effects on multiple mitochondrial functions. Moreover, we profiled aging-associated redox landscape changes of the mitochondrial cysteinome in multiple tissues, and importantly, revealed that ROMO1 counteracts the mitochondrial cysteinome oxidations and retards functional decline of organs during aging.

https://doi.org/10.1038/s41467-025-60503-z

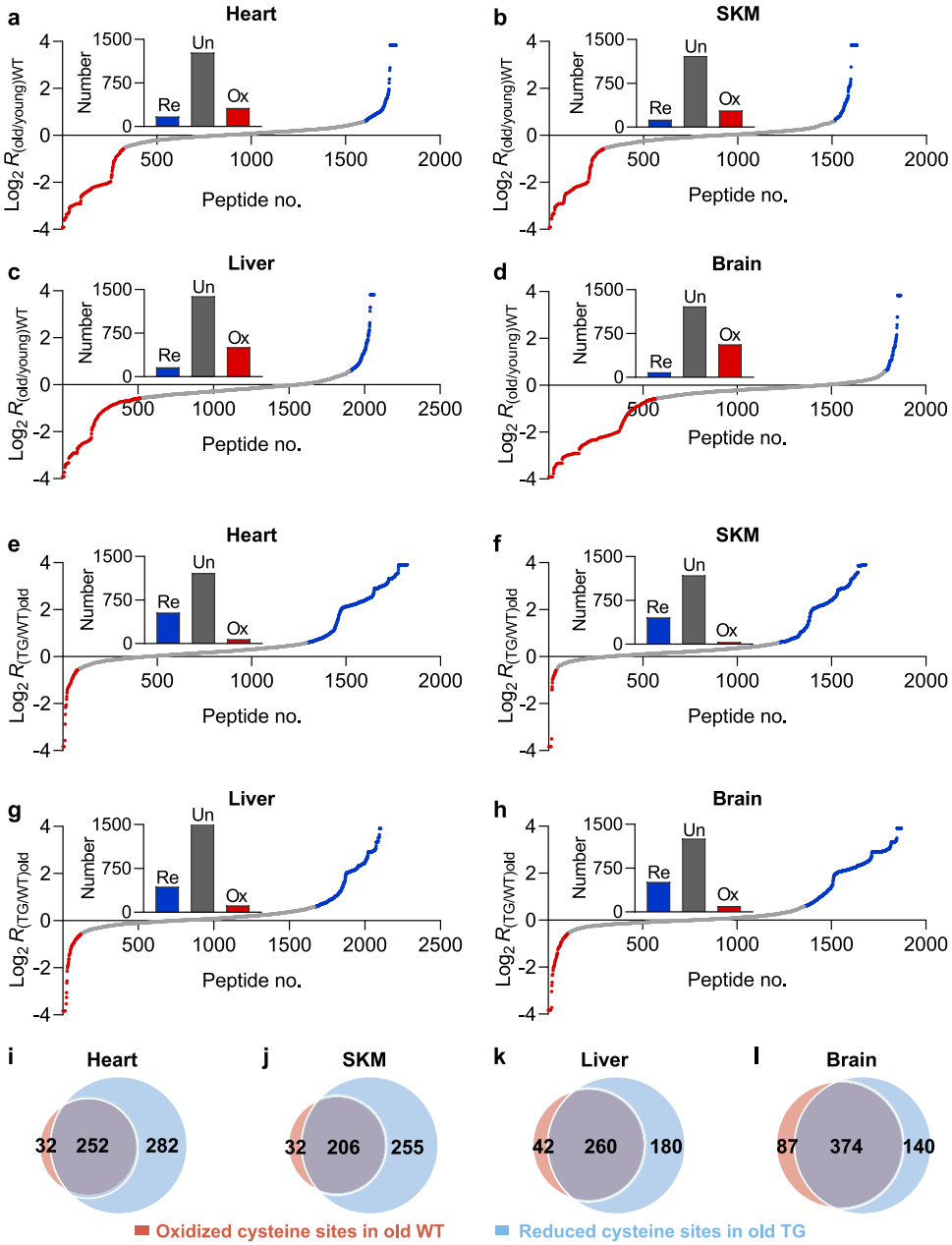


**Fig. 6 | ROMO1 upregulation reverses aging-associated oxidations of the mitochondrial cysteinome in multiple organs. a–d** Distributions of the averaged activity-based protein profiling ratios of $Old_{(WT)}/Young_{(WT)}$ of the mitochondrial cysteinome in the heart (**a**), skeletal muscle (SKM) (**b**), liver (**c**) and brain (**d**). Blue, gray, and red dots indicate the reduced ($Log_2R_{(old/young)} \geq 0.58$), unchanged ($-0.58 < Log_2R_{(old/young)} < 0.58$), and oxidized ($Log_2R_{(old/young)} \leq -0.58$) cysteine sites in the old WT mitochondria, respectively. Insets show numbers of cysteine sites being reduced (Re), unchanged (Un), and oxidized (Ox). $n = 4$ independent experiments from 8 mice for each tissue (4 M 4 F for each group). 3-month-old (young) and 25-month-old (old) WT mice were used. **e–h**, As in (**a–d**), except the averaged activity-based protein profiling ratios were $Log_2R(TG_{old}/WT_{old})$. $n = 4$ independent experiments from 8 mice for each tissue (4 M 4 F for each group). 25-month-old WT and TG mice were used. **i–l** Venn diagram showing the overlap between the oxidized cysteine sites during aging in WT tissues ($Log_2R_{(Old/Young)WT} \leq -0.58$) and the reduced cysteine sites by ROMO1 upregulation in aged tissues ($Log_2R_{(TG/WT)old} \geq 0.58$). Source data are provided as a Source Data file.

We demonstrate that ROMO1, as a small, ubiquitous, and IMM-delimited protein effectively protects the mitochondrial cysteinome from oxidations. The ROMO1 redox-protected mitochondrial proteins permeate OMM, IMS, and IMM as well as the matrix. We speculate that ROMO1 protects its target protein thiols through dual mechanisms of action. On one hand, ROMO1 may directly detoxify ROS, thereby enabling it to protect a wide-spectrum of mitochondrial proteins which are extensively distributed in different mitochondrial compartments. On the other hand, ROMO1 may preemptively form reversible intermolecular disulfides with its oxidized target proteins to prevent their deleterious oxidations.

We suggest that mitochondrial GSH- and TRX2-reducing systems could participate in the recycling of reactive thiols of both ROMO1 and its target cysteines which form intermolecular disulfide with it. We pinpointed ROMO1 C15 and C42 as functionally essential sites for its thiol-protection and functional phenotypes. Mutation of either, but not C27 and C79, disabled ROMO1 in protecting functional thiols and the resultant beneficial impacts including inhibiting mPTP opening and augmenting mitochondrial $Ca^{2+}$ uptake activity.

Our in vitro assay shows that purified ROMO1 detoxifies $H_2O_2$ with a relatively low rate constant, which is significantly slower than the canonical peroxide-degrading enzymes. But the isolated

https://doi.org/10.1038/s41467-025-60503-z

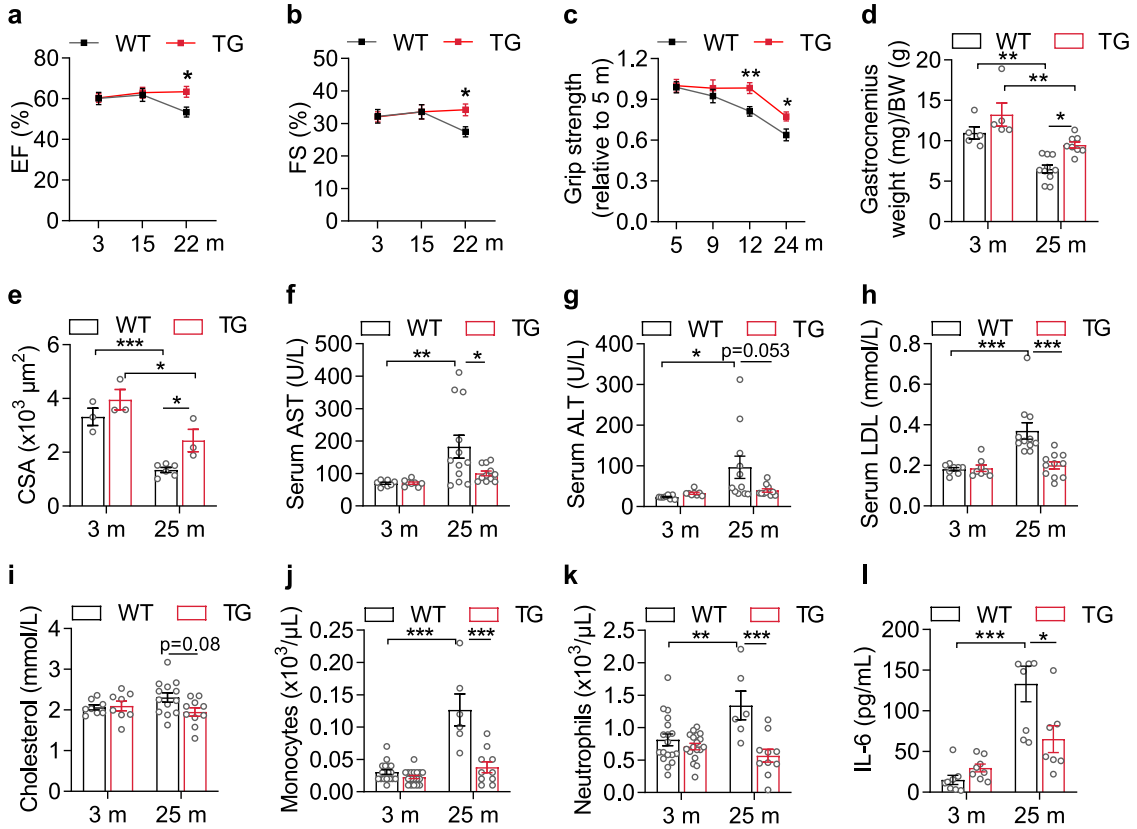


**Fig. 7 | ROMO1 upregulation retards functional decline of multiple organs during aging. a, b** Echocardiographic analysis of heart functions in WT and TG mice at the age of 3, 15, and 22 months (m). EF, injectional fraction; FS, fractional shortening. Data are mean ± s.e.m. In **a**, for 3-month old mice, $n = 12$ (6 M 6 F) in WT and $n = 13$ (7 M 6 F) in TG; for 15-month old mice, $n = 8$ (4 M 4 F) in WT and $n = 11$ (7 M 4 F) in TG; for 22-month old mice, $n = 5$ (3 M 2 F) in WT and $n = 5$ (3 M 2 F) in TG. In **b**, for 3-month old mice, $n = 12$ (6 M 6 F) in WT and $n = 13$ (7 M 6 F) in TG; for 15-month old mice, $n = 8$ (4 M 4 F) in WT and $n = 8$ (5 M 3 F) in TG; for 22-month old mice, $n = 5$ (3 M 2 F) in WT and $n = 5$ (3 M 2 F) in TG. **c** Relative changes of grip strength of WT and TG male mice at different ages. Data are mean ± s.e.m. For 5-month-old mice, $n = 12$ in WT and $n = 15$ in TG; for 9-month-old mice, $n = 12$ in WT and $n = 12$ in TG; for 12-month-old mice, $n = 10$ in WT and $n = 11$ in TG; for 24-month-old mice, $n = 7$ in WT and $n = 9$ in TG. **d** Attenuated gastrocnemius muscle loss in old TG mice. Data are mean ± s.e.m. For 3-month-old mice, $n = 5$ in WT and $n = 5$ in TG; for 25-month-old mice, $n = 10$ in WT and $n = 8$ in TG. Male mice were used. BW, body weight; mg, milligram; g, gram. **e** Cross-sectional area (CSA) analysis of gastrocnemius muscle fiber in 3-month and 25-month-old WT and TG mice. Data are mean ± s.e.m. For 3-month-old mice, $n = 3$ in WT and $n = 3$ in TG; for 25-month-old mice, $n = 6$ in WT and $n = 3$ in TG. Male mice were used. **f**–**i** Analysis of serum biomarkers in young and old WT and TG mice. AST, aspartate aminotransferase; ALT, alanine aminotransferase; LDL, low-density lipoprotein. Data are mean ± s.e.m. In **f**, $n = 8$ WT and $n = 8$ TG 3-month-old mice; $n = 12$ WT and $n = 11$ TG 25-month-old mice. In **g** and **h**, $n = 8$ WT and $n = 8$ TG 3-month-old mice; $n = 11$ WT and $n = 11$ TG 25-month-old mice. In **i**, $n = 8$ WT and $n = 8$ TG 3-month-old mice; $n = 13$ WT and $n = 10$ TG 25-month-old mice. Male mice were used. **j**-**l**, Number of blood monocytes (**j**) and neutrophils (**k**) and circulating interleukin-6 (IL-6) level (**l**) in young and old WT and TG mice. Data are mean ± s.e.m. In **j**, **k**, $n = 18$ WT and $n = 18$ TG 3-month-old mice; $n = 6$ WT and $n = 10$ TG 25-month-old mice. In **l**, $n = 8$ WT and $n = 8$ TG 3-month-old mice; $n = 8$ WT and $n = 7$ TG 25-month-old mice. Male mice were used. In **a**–**c**, two-tailed unpaired Student's *t*-test with Welch's correction was used; in **d**–**l**, two-way ANOVA with Tukey's multiple comparisons test was used. $^*p < 0.05$, $^{**}p < 0.01$, $^{***}p < 0.001$. Source data are provided as a Source Data file.

mitochondrial data reveal that overexpression of ROMO1 effectively eliminates $H_2O_2$ in situ. We speculate that this biological significance might be attributed to a high local concentration of ROMO1 in IMM, given that $H_2O_2$ elimination capacity depends on both the rate constant and antioxidant concentration. Since IMM is the primary site of mitochondrial ROS production by electron transfer chain, such IMM-localized enrichment may also enable ROMO1 to detoxify ROS wherein they are produced. Further, the recycling systems, such as GSH- and TRX2-reducing systems, may sustain high local abundance of reactive ROMO1 in IMM by effectively reducing oxidized ROMO1 back.

An alternative explanation is that ROMO1 may have indirect effects on mitochondrial ROS. It has previously been reported that ROMO1 is required for mitochondrial fusion and normal cristae morphology[28]. It is possible that differences in ROS accumulation and cysteine oxidation. At this stage we cannot distinguish between direct effects of ROMO1 (i.e. forming disulfide bonds with target proteins and direct detoxification of ROS) and indirect effects due to changes in mitochondrial morphology or function.

By further profiling the redox landscape of the mitochondrial cysteinome in tissues from old animals, we showed a dramatic oxidative shift of the mitochondrial cysteinome in line with the decreased expression of ROMO1. ROMO1 upregulation not only shifted the mitochondrial cysteinome to a reductive state in young tissues, but also reversed its aging-associated shift toward oxidation. This result provides direct evidence supporting the prevailing hypothesis that accumulated oxidations might happen on the proteome due to increased ROS in aging[11,54,55]. Notably, a number of tissue-specific and aging-related disease driver proteins were identified to be selectively oxidized in the old mice, suggesting a possible link between oxidative modifications of these mitochondrial proteins and aging-associated functional declines in a given organ. This idea is substantiated by the finding that ROMO1 upregulation counteracts oxidations of these disease driver proteins and, more importantly, systematically prevented aging-associated functional declines of organs examined (heart, skeletal muscle and liver). These results are consistent with that oxidative damage contributes to many aging-associated pathologies[55,56].

At the organelle level, we demonstrated that the mitochondria with a more reductive cysteinome operate more efficiently and become more robust in stressful conditions. We showed that thiol-protection by ROMO1 exerted beneficial effects on all aspects of mitochondrial functions examined, including enhancing energy metabolism, inhibiting membrane permeability transition, and promoting mitochondrial $Ca^{2+}$ uniport. Given that the respiratory chain is the primary site of both ATP production and ROS generation[12,57], it is critical and challenging for the respiratory complexes to avoid ROS attacks during energy metabolism. In this regard, ROMO1 protects 69 cysteine sites on 29 subunits of Complexes I-V, and accordingly, mitochondrial respiration is largely enhanced by ROMO1 upregulation and repressed by ROMO1 ablation. ROMO1 has been implicated in affecting ROS production with conflicting results reported in different cells[21–28]. The discrepancy in ROS production could be attributable to the variety in ROS metabolism for different cell types. Considering the thiol-protection of respiratory chain complex subunits by ROMO1, it is also likely that these contradictory effects on ROS production might be due to that altering ROMO1 expression affects the redox state of disparate cysteine sites in different cells.

The beneficial impact of ROMO1 thiol-protection was also exemplified by inhibition of mPTP opening induced by either $Ca^{2+}$ overload or oxidative stress. In consistent with the dependence of C15 and C42 rather than C27 or C79 for ROMO1 thiol-protection, these two cysteine sites are required for suppression of mPTP activity by ROMO1. Although the molecular identities of mPTP are still in debate[40], our results suggest ROMO1 as a strong negative regulator of mPTP opening, and underscore the importance of altering cysteine redox states in regulating mPTP activity. Since mPTP opening is involved in a plethora of pathological events such as ischemic injuries in the heart and brain[58], that ROMO1 inhibits mPTP activity affords a new insight for retarding such desperate mitochondrial damages.

The ABPP analysis used in the current study provides an overall redox modification profile of the mitochondrial cysteinome, but with some technical limitations. It can neither quantify the extent to which a cysteine site is oxidized nor discriminate the cysteine modification types. Recently, Xiao and Jedrychowski et al. developed an Oximouse approach to quantitatively assess the aggregate modification state of all the reversible cysteine modifications of the whole-tissue proteome[59]. Future investigations that combine these complementary approaches might provide quantitative and oxidation type-specific analyses of the redox landscape of the mitochondrial cysteinome in diverse physiological and pathological conditions.

In summary, our findings underscore the importance of ROMO1, an IMM-delimited small protein, in protecting the mitochondrial cysteinome against oxidations. A series of questions remain to be answered, e.g., how ROMO1 expression is regulated under physiological and pathological conditions, how *ROMO1* mutations are correlated with human diseases, and whether ROMO1 can react with different types of ROS. Nonetheless, it is tempting to speculate that, by reinforcing or mimicking ROMO1 thiol-protection, it might provide a strategy for treating oxidative stress-related pathologies and extending healthspan and lifespan.

## Methods

### Animal study approval

All experiments involving animals conformed to the rules of the Association for Assessment and Accreditation of Laboratory Animal Care (AAALAC) and the Guide for the Care and Use of Laboratory Animals published by the US National Institutes of Health (NIH Publication eighth edition, update 2011). All procedures were approved by the Animal Care Committee of Peking University (IMM-ChengHP-1, 14) and PKU-Nanjing Institute of Translational Medicine (IACUC-2021-023). All mice were housed in a temperature-controlled (20-22 °C) and specific pathogen-free animal facility, 3-5 per cage, and maintained on a 12-h light/dark cycle, with water and food available *ad libitum*.

### Generation of *Romo1* pan-tissue transgenic mouse model

The mouse *Romo1* cDNA sequence (NM_025946) was cloned into the pUCCAGGS plasmid downstream of the chicken β-actin promoter. The construct was linearized with *Sal*I and *Stu*I to release the transgenic cassette. After sequencing confirmation, the purified fragment was microinjected into fertilized eggs of C57BL/6 J mice (JAX stock 000664). Three lines were initially constructed and analyzed, and a single line was subsequently used for experiments. Genotypes of transgenic offspring were confirmed by polymerase chain reaction (PCR) using tail DNA. Mouse PCR primer sequences are provided in Supplementary Data 4.

### Generation of *Romo1* knockout mouse models

Floxed *Romo1* mice were generated by standard techniques using a targeting vector containing a neomycin resistance cassette flanked by FRT sites. Briefly, exon 2 of the *Romo1* gene was inserted into two flanking *loxP* sites. After electroporation of the targeting vector into embryonic stem (ES) cells v6.5 (C57BL/6×129S4/SvJae F1), G418-resistant ES cells were screened for homologous recombination by Southern blot. Heterozygous ES clones were identified and microinjected into blastocysts of C57BL/6 J mice to generate heterozygous germline-transmitted floxed mice (*Romo1*$^{f/+}$). Homozygous *Romo1*-floxed mice (*Romo1*$^{f/f}$) were obtained by inbreeding the *Romo1*$^{f/+}$ mice.

To generate global *Romo1* knockouts, *Romo1*$^{f/f}$ mice were crossed with Prm-Cre transgenic mice (129S/Sv-Tg(Prm-Cre)58Og/J, JAX stock 003328), in which Cre recombinase is expressed in the male germ line under the control of the protamine 1 promoter, to get *Romo1*$^{+/-}$ mice. And the heterozygous knockouts were intercrossed to generate homozygous *Romo1*$^{-/-}$ mice. PCR was performed to confirm the genotypes. Mouse PCR primer sequences are provided in Supplementary Data 4.

Cardiomyocyte-specific *Romo1* knockout mice were generated as previously described[60]. Briefly, mice homozygous for floxed *Romo1* allele were crossed with MLC2v-Cre transgenic mice, in which the Cre recombinase is placed under the promoter of the myosin light chain 2v which is specifically expressed in ventricular cardiomyocytes[61,62]. The resulting double heterozygous MLC2v-Cre$^{+}$/*Romo1*$^{f/+}$ mice were then backcrossed with *Romo1*$^{f/f}$ mice to generate MLC2v-Cre$^{+}$/*Romo1*$^{f/f}$ cardiomyocyte-specific *Romo1* knockouts and MLC2v-Cre$^{-}$/*Romo1*$^{f/f}$ littermate controls. Genotyping was performed by PCR analysis of tail DNA using Cre-specific primers and primers spanning intron 1 and exon 2 of the *Romo1* gene. Mouse PCR primer sequences are provided in Supplementary Data 4.

Hepatocyte-specific *Romo1* knockout mice were generated by inducing Cre recombinase expression under the control of the promoter of thyroxine binding globulin (TBG) which is exclusively expressed in the hepatocytes[63,64]. Briefly, 5-7 weeks old *Romo1*$^{f/f}$ mice were injected with adeno-associated virus (AAV) via tail intravenous administration (AAV8-TBG-GFP for control and AAV8-TBG-Cre for knockout). AAVs were injected with $1\times10^{11}$ vector genomes per mouse at least 2 weeks before the experiments. ROMO1 depletion was confirmed by immunoblotting.

### Generation of cardiomyocyte-specific *Romo1* C15S or C42S knockin mouse models

cDNA encoding mouse *Romo1*(C15S) or *Romo1*(C42S) mutant was subcloned into a CRISPR/Cas9-mediated homologous recombination vector targeting the *Rosa26* locus and injected into single cell embryos of C57BL/6 J mice. The transgene is driven by the EF1A promoter and is interrupted by a *loxP*-stop (3×polyA signal)-*loxP* cassette to render its expression inducible by Cre recombinase. Then, the transgenic mice with correct insertion were intercrossed with the *Romo1*$^{f/f}$ mice to generate homologous EF1A-*loxP*-stop-*loxP*-*Romo1*(C15S or C42S)/*Romo1*$^{f/f}$ mice. AAVs carrying the Cre gene under the control of the cardiac troponin T promoter (AAV9-cTNT-GFP for control and AAV9-

cTNT-Cre for knockin, $5\times10^{11}$ vector genomes per mouse) were administered at 5-7 weeks of age via tail intravenous injection to induce cardiomyocyte-specific expression of mutant ROMO1(C15S) or ROMO1(C42S) and simultaneous deletion of endogenous ROMO1. Experiments were performed at least 2 weeks after AAV delivery. Expression of ROMO1(C15S) or ROMO1(C42S) protein was confirmed by immunoblotting.

### Cell culture and plasmid transfection

Human cell lines HeLa and HEK293T were purchased from the ATCC and cultured in Dulbecco's Modified Eagle's Medium (DMEM) supplemented with 10% (vol/vol) fetal bovine serum (FBS) and 1% (vol/vol) penicillin/streptomycin in a humidified incubator at 37 °C with 5% $CO_2$. For plasmid transfection, cells were transiently transfected with the indicated plasmids using Lipofectamine™ 2000 according to the manufacturer's protocol. Confocal imaging and Western blot analysis were performed 48–72 h after plasmid transfection.

### Isolation and culture of adult rodent cardiomyocytes

Mouse ventricular myocytes were isolated as described previously[65]. Briefly, excised mouse hearts were perfused for 1 min at 37 °C with perfusion buffer containing 120 mM NaCl, 5.4 mM KCl, 1.2 mM $NaH_2PO_4$•$2H_2O$, 1.2 mM $MgCl_2$•$6H_2O$, 5.6 mM D-glucose, 5 mM taurine, 10 mM 2,3-butanedione 2-monoxime, and 10 mM HEPES, pH 7.35. Hearts were then recirculated for 20 min with perfusion buffer supplemented with collagenase (1 mg/mL, type II). The left ventricle was then dissected and minced, and the cardiomyocytes were allowed to sediment by gravity. Calcium reintroduction was performed stepwise from 20 µM to 1 mM. Freshly isolated cardiomyocytes suspended in the perfusion buffer were plated on laminin-coated culture dishes for 1 hour, and the attached cells were then maintained in DMEM supplemented with 10% FBS and 10 mM 2,3-butanedione 2-monoxime.

Adult rat cardiomyocytes were isolated from male Sprague-Dawley rats (200-250 g) following a standard enzymatic digestion protocol. Briefly, excised hearts were perfused for 5 min at 37 °C with $Ca^{2+}$-free Tyrode's solution containing 137 mM NaCl, 5.4 mM KCl, 1.2 mM $MgCl_2$•$6H_2O$, 1.2 mM $NaH_2PO_4$•$2H_2O$, 20 mM HEPES, 5.6 mM D-glucose and 10 mM taurine, pH 7.35. Hearts were then recirculated for 60 min with Tyrode's solution supplemented with collagenase (0.5 mg/mL, type II) and protease (0.06 mg/mL, type XIV). Ventricles were minced and shaken 2–3 times at 2 *g* for 4 min in the same solution. The dislodged cells were centrifuged at 4 *g* for 40 seconds. The pellet was resuspended in Tyrode's solution containing 1 mg/mL bovine serum albumin (BSA) and 50 µM $CaCl_2$. Calcium reintroduction was then performed stepwise from 50 µM to 1 mM. Freshly isolated cardiomyocytes suspended in M199 medium were plated on laminin-coated culture dishes for 1 hour, and the attached cells were then maintained in M199 medium supplemented with 1 mg/mL BSA and 1×insulin-transferrin-selenium. For adenovirus infection, cultured cardiomyocytes were infected with the indicated adenovirus at a multiplicity of infection of 20.

### Isolation and culture of neonatal rat ventricular cardiomyocytes (NRVMs)

NRVMs were isolated from 0-1-day-old Sprague-Dawley rat pups. Ventricles were harvested, rinsed and minced into small fragments, and then transferred to digestion solution (HBSS buffer containing 1 mg/mL trypsin and 0.8 mg/mL type II collagenase). Repeated digestions were performed at 37 °C for 5 min each round in a spinning flask until most of the NRVMs were dissociated into suspension. After each round of digestion, the supernatant was collected, and the cells were pelleted by centrifugation at 60 *g* for 5 min. According to the different attachment ability, cardiac fibroblasts were minimized by pre-plating for 2 hours and the unattached cardiomyocytes were then collected and diluted in DMEM supplemented with 10% FBS and 0.1 mM 5-bromo-2'-deoxyuridine. NRVMs were synchronized for 48 hours before treatment. Cell preparations typically contained more than 95% cardiomyocytes. For adenovirus infection, cultured NRVMs were infected with the indicated adenovirus at a multiplicity of infection of 20.

### Isolation and culture of adult mouse primary hepatocytes

Primary hepatocytes were isolated 2 weeks post AAV injection. Through the portal vein, the liver was perfused with 50 mL Krebs Ringer with Glucose buffer to remove the residual blood and then perfused with 30 mL Krebs Ringer with Glucose buffer containing collagenase (1 mg/mL, type IV). The liver was immediately removed from the mice, cut into small pieces, and filtered through a 70-µm cell strainer to remove tissue debris. The filtered solution was washed with cold DMEM and centrifuged 3 times at 50 *g* for 4 min. The isolated hepatocytes were resuspended in DMEM containing 10% FBS and 1% penicillin/streptomycin.

### APEX2 proximity labeling and electron microscopy

HEK293T cells untransfected or stably expressing ROMO1-APEX2 or APEX2-ROMO1 fusion protein were grown to 90% confluence and fixed with 2.5% glutaraldehyde at room temperature, then quickly transferred to ice. After 30-60 min, cells were rinsed in chilled buffer (100 mM sodium cacodylate, 2 mM $CaCl_2$, pH 7.4) and then treated for 5 min in the same buffer containing 20 mM glycine to quench unreacted glutaraldehyde, followed by rinses in chilled buffer. A freshly diluted solution of 0.5 mg/mL diaminobenzidine free base combined with 10 mM $H_2O_2$ was added to the cells for 5 min. The solution was then removed, and the cells were rinsed again. Post-fixation staining was performed with 2% osmium tetroxide for 30 min in chilled buffer. Cells were rinsed in chilled distilled water and then placed in chilled 2% uranyl acetate overnight. Samples were then centrifuged at 700 *g* for 1 min to generate a cell pellet. The pellets were dehydrated in a graded ethanol series (50%, 75%, 90%, 95%, 100%, 100%, 100%), 10 min for each concentration, then infiltrated in EMBED-812 using 1:1 (vol/vol) resin and anhydrous ethanol overnight, followed by two changes to 100% resin before leaving the samples overnight. Finally, each sample was rinsed again with 100% resin before transfer to fresh resin and polymerization at 60 °C for 48 hours. Embedded cell pellets were cut into 50-nm sections and imaged on a FEI-Tecnai G2 20 Twin transmission electron microscope operated at 120 kV.

### Determination of ROMO1 midpoint redox potential ($E_m$)

ROMO1-FLAG protein (3 µg/sample) expressed and purified from HEK293T cells was incubated and equilibrated in basal redox buffers (50 mM Tris-HCl and 1 mM EDTA, pH 7.5) in the presence of 100 mM trans-4,5-dihydroxy-1,2-dithiane (oxidized DTT) and various concentrations of DL-dithiothreitol (reduced DTT) at 25 °C for 16 hours under a nitrogen atmosphere. Notably, the buffers were thoroughly degassed to minimize oxidation by air. After incubation, the samples were precipitated with ice-cold acetone, washed once with 80% ice-cold acetone, and then dissolved in basal buffer containing 50 mM mPEG2K-MAL and 2% SDS for mPEG2K-MAL labeling with incubation for 30 min at 37 °C. The proteins were again precipitated with ice-cold acetone and suspended in 1×SDS loading buffer (62.5 mM Tris-HCl, 1 mM EDTA, 2% SDS, 0.1% bromophenol blue and 33% glycerol, pH 7.5). After separation in 12% Tricine SDS-PAGE, the differentially mPEG2K-MAL-labeled ROMO1 was stained with Coomassie brilliant blue (CBB) R-250, imaged using an Odyssey imaging system (LI-COR), and quantified using ImageJ. The reduced level of ROMO1, calculated as the ratio of the reduced form to the total protein, was plotted against the redox potential of DTT buffer (as a reference, the standard redox potential of DTT at pH 7.5 was -357 mV). The data were fitted to the Nernst equation and $E_m$ values corresponding to the oxidation of one, two, three, and four cysteines were calculated.

### In vitro $H_2O_2$ detoxification assay

Amplex® Red hydrogen peroxide assay kit (catalogue no. A22188, invitrogen™) was used to determine $H_2O_2$ concentration according to the manufacturer's instructions. Briefly, 2 μM freshly prepared $H_2O_2$ was added to the solutions containing different concentrations (0-2 μM) of purified recombinant human WT ROMO1, ROMO1-FLAG or mutant ROMO1-FLAG (4CS) protein, and then immediately measured after quickly mixing within 30 seconds. The final concentrations of $H_2O_2$ were retrieved by comparing to standard curve.

To assess kinetics of ROMO1-mediated $H_2O_2$ elimination, different concentrations of $H_2O_2$ were incubated with 2 μM purified ROMO1-FLAG protein or sample buffer at room temperature and measured immediately within 30 seconds after rapid mixing. The final concentrations of $H_2O_2$ were determined by comparison to a standard curve. Note that estimation of the rate constant assumes ROMO1 consumed the corresponding amount of $H_2O_2$ in 30 seconds, which is constrained by our measurement limits, as the shortest reaction duration we can effectively monitor is 30 seconds. Additionally, it should be noted that the purified ROMO1 protein cannot be 100% in the reductive state theoretically.

### In vitro coupled spectrophotometric assay for the kinetic analysis of reducing oxidized ROMO1

The kinetic analysis of reducing oxidized ROMO1-FLAG by GSH- or TRX2-reducing system was performed using a coupled spectrophotometric assay, in which the continuous reduction of pre-oxidized ROMO1-FLAG depends on the recycling of GSH by glutathione reductase (GR) or of reduced TRX2 by thioredoxin reductase (TrxR), which is coupled to the consumption of the ultimate reducing equivalent, NADPH, and is monitored spectrophotometrically at 340 nm[66–69]. Pre-oxidized ROMO1 was prepared by incubating purified ROMO1-FLAG protein with a 10-fold molar excess of $H_2O_2$ for 30 minutes at room temperature. Excess $H_2O_2$ was then removed using a 7-kDa molecular weight cutoff spin column, and the concentration of ROMO1-FLAG was re-determined using Pierce BCA protein assay for subsequent kinetic analysis experiments. For GSH-mediated reduction, the reaction system contained different concentrations of oxidized ROMO1, 1 mM freshly prepared GSH, 0.2 μM GR, and 1 mM NADPH in a buffer consisting of 50 mM Tris-HCl and 2 mM EDTA (pH 7.5). In TRX2-reaction system, different concentrations of oxidized ROMO1, 5 nM freshly reduced TRX2-FLAG, 0.5 μM TrxR-FLAG, and 0.3 mM NADPH were used. A microplate reader was used to record the 340 nm absorbance in a 96-well plate containing a 50 μL reaction volume. The optical path length is 0.16 cm. The initial NADPH consumption rate was calculated from the slope of the progress absorbance curve at the beginning of the reaction, using the extinction coefficient of NADPH (6220 $M^{-1}cm^{-1}$). The calculated initial NADPH consumption rate was then plotted against different concentrations of oxidized ROMO1 and the kinetic parameters were determined by fitting the data using GraphPad Prism v9.0.0 software.

### In vitro formation and reduction of ROMO1 homodimers

For detecting disulfide-bonded homodimer of ROMO1, purified human recombinant WT or mutant ROMO1-FLAG protein (3.6 μg) was incubated with 10 μM $H_2O_2$ for 30 minutes at room temperature. The resulting mixtures were then analyzed using non-reducing SDS-PAGE stained with CBB or for the subsequent reduction assay.

For the reduction of disulfide-bonded homodimer of ROMO1, after incubation with $H_2O_2$ as above, excess $H_2O_2$ was removed using a 7-kDa molecular weight cutoff spin column. The resulting pre-oxidized ROMO1-FLAG were then incubated with a GSH reduction system containing 1 mM freshly prepared GSH, 0.2 μM GR, and 1 mM NADPH, or with a TRX2 reduction system containing 0.5 μM freshly reduced TRX2-FLAG, 0.5 μM TrxR-FLAG, and 0.3 mM NADPH for 30 minutes at 37 °C. The samples were subsequently analyzed by non-reducing SDS-PAGE stained with CBB.

### In vitro formation and reduction of intermolecular disulfides

For intermolecular disulfides formed between ROMO1 and its client proteins, purified human recombinant ROMO1-FLAG protein (3.6 μg) was incubated with the purified human SDH complex (5.0 μg), MCU-FLAG (3.6 μg), or ANT2-FLAG (4.0 μg) for 20 h at 4 °C in the absence or presence of 100 μM $H_2O_2$, respectively. The samples were then analyzed by non-reducing SDS-PAGE stained with CBB or for reduction assay.

For the reduction of disulfide-bonded heterodimer of ROMO1-SDHA, after incubating ROMO1 and SDH complex with $H_2O_2$ as described above, excess $H_2O_2$ was removed for the pre-incubated mixtures using a 7-kDa molecular weight cutoff spin column. The resulting pre-oxidized mixtures were then incubated with a GSH reduction system containing 1 mM freshly prepared GSH, 0.2 μM GR, and 1 mM NADPH, or with a TRX2 reduction system containing 0.5 μM freshly reduced TRX2-FLAG, 0.5 μM TrxR-FLAG, and 0.3 mM NADPH for 30 minutes at 37 °C. The samples were subsequently analyzed by non-reducing SDS-PAGE stained with CBB.

### Non-reducing SDS-PAGE

Protein samples were treated with modified Laemmli sample buffer (62.5 mM Tris-HCl, 2% SDS, 10% glycerol, 60 mM N-ethylmaleimide, 0.002% Bromphenol blue, no DTT, no β-mercaptoethanol, pH 6.8). To facilitate thiol alkylation and prevent thiol-disulfide exchange, 6% (vol/vol) of 1 M N-ethylmaleimide was added to the modified Laemmli sample buffer at the very beginning. Protein samples were separated by 10-16% tricine or glycine SDS-PAGE and visualized using CBB staining or subjected to Western blot analysis.

### Mass spectrometric profiling of intermolecular disulfide bonds

The complex bands in the non-reducing SDS-PAGE gel were cut out and destained. Then the samples were fourfold diluted with 50 mM $NH_4HCO_3$, and digested with trypsin at a 1:50 enzyme/substrate ratio at 37 °C for 12 hours. After digestion, the samples were centrifuged at 12,000 *g* for 10 min and the supernatants were dried by vacuum centrifugation. Dried samples were resuspended in 0.1% formic acid (FA) and then desalted using C18 stage tips. Digested peptides were then eluted with 50% acetonitrile and 0.1% FA. Eluted peptides were dried by vacuum centrifugation, resuspended in 0.1% FA and subjected to LC–MS/MS analysis to identify the presence of disulfide bonds. For disulfide bonds identification, the raw data file was searched against the database consisting of the sequences of ROMO1, SDHA, MCU and ANT2. Database searches were performed with pLink studio (version 2, http://pfind.ict.ac.cn/software/pLink/index.html). The parameters for pLink-SS search were as follows: flow type is Disulfide Bond (HCD-SS); the set linker is SS; the enzyme was set as trypsin or semi-trypsin; the maximum number of modifications and missed cleavages allowed per peptide were three; peptide length range is 4–60 amino acids; peptide mass range is 300–6,000; precursor ion mass and fragmentation tolerance were 10 ppm and 20 ppm, respectively; mass shift of +125.047 Da (N-ethylmaleimide[C]) was searched as variable modification. For spectra preprocessed by pParse, the requirement was no more than 10 ppm deviations from the monoisotopic mass. Candidate disulfide-linked peptides were identified with relaxed database search (semi-digestion) and filtered with an E-value cut-off of 0.01 and a false discovery rate cut-off of 0.05.

### Mitochondrial isolation and mitoplast preparation

Briefly, mouse tissues were extracted and washed in ice-cold phosphate-buffered saline (PBS), and then minced and homogenized on ice in mitochondrial isolation buffer (210 mM mannitol, 70 mM sucrose, 1 mM EGTA, 0.1% fatty acid-free BSA, and 10 mM HEPES, pH 7.2) using a pre-chilled glass Dounce tissue grinder (10-25 strokes depending on the tissue type and weight). For isolation of cardiac, skeletal muscle, and brain mitochondria, homogenates were centrifuged at 4 °C for 10 min at 700 *g*. The supernatants were then collected and further

centrifuged at 4 °C for 10 min at 12,000 *g*. The pellets were resuspended in mitochondrial isolation buffer for further assessment. For isolation of liver mitochondria, the homogenate was centrifuged at 4 °C for 10 min at 1000 *g*, and the supernatant was collected and further centrifuged at 4 °C for 15 min at 3500 *g*. For mitoplast preparation, isolated mitochondria were osmotically swollen by incubation in 20 mM Tris-HCl (pH 7.4) solution for 20 min on ice and then centrifuged at 4 °C for 10 min at 12,000 *g*. The pellet was retained for further experiments. For membrane protein analysis, mitochondrial pellets were resuspended in 0.1 M $Na_2CO_3$, pH 11.5, sonicated, and incubated on ice for 30 min. Insoluble membrane fractions were sedimented by centrifugation at 100,000 *g* for 10 min, and the soluble supernatant was retained for further analysis.

### Analysis of mitochondrial aconitase activity

Mitochondrial aconitase activity was measured using the commercially available aconitase activity assay kit. In brief, 50 μg isolated cardiac mitochondria or 100 μg liver mitochondria were added to each well of a 96-well plate containing the assay buffer with isocitrate. Aconitase activity was indexed by the increase of $OD_{240nm}$ which indicates the conversion of isocitrate to *cis*-aconitate. Reaction rates were calculated by analyzing the linearly increasing section. For $H_2O_2$ treatment, $H_2O_2$ was added to the assay buffer at the initiation of the measurement to a final concentration of 50 μM for heart mitochondria or 200 μM for liver mitochondria.

### Western blot

Fresh or frozen tissue or cell pellets were lysed in denaturing lysis buffer (150 mM NaCl, 1% Triton X-100, 0.5% sodium deoxycholate, 0.1% SDS, and 50 mM Tris-HCl, pH 7.4) containing protease/phosphatase inhibitors, separated by 10-16% tricine or glycine SDS-PAGE, and transferred to PVDF membranes (0.22 μm). After blocking with 5% nonfat milk in TBST solution (1.5 M NaCl, 100 mM Tris, 0.1% Tween-20, pH 7.35), the membranes were incubated with primary antibodies diluted in 5% nonfat milk TBST solution overnight at 4 °C. The antibodies used include anti-ROMO1 (1:2000 dilution, catalogue no. TA505612, OriGene), anti-ATPB (1:2000 dilution, catalogue no. ab14730, Abcam), anti-ATP5A (1:2000 dilution, catalogue no. ab14748, Abcam), anti-SDHA (1:2000 dilution, catalogue no. ab137040, Abcam), anti-β-Actin (1:5000 dilution, catalogue no. AC026, Abclonal), anti-SOD1 (1:1000 dilution, catalogue no. A0274, Abclonal), anti-TRX2 (1:1000 dilution, catalogue no. A6782, Abclonal), anti-GPX4 (1:1000 dilution, catalogue no. A11243, Abclonal), anti-PRDX5 (1:1000 dilution, catalogue no. A1269, Abclonal), anti-NDUFA8 (1:1000 dilution, catalogue no. ab184952, Abcam), anti-NDUFA9 (1:1000 dilution, catalogue no. ab128744, Abcam), anti-NDUFS1 (1:1000 dilution, catalogue no. ab169540, Abcam), anti-UQCRC1 (1:1000 dilution, catalogue no. ab110252, Abcam), anti-UQCRFS1 (1:1000 dilution, catalogue no. ab14746, Abcam), anti-MTCO1 (1:1000 dilution, catalogue no. ab14705, Abcam), anti-SOD2 (1:2000 dilution, catalogue no. ab68155, Abcam), anti-TIM23 (1:1000 dilution, catalogue no. ab230253, Abcam), anti-GAPDH (1:2000 dilution, catalogue no. A19056, Abclonal), anti-MCU (1:500 dilution, catalogue no. D2Z3B, Cell Signaling Technology), anti-MICU1 (1:500 dilution, catalogue no. D4P8Q, Cell Signaling Technology), anti-DDK (FLAG) (1:2000 dilution, catalogue no. TA50011-100, OriGene), anti-biotin (1:2000 dilution, catalogue no. A20684, Abclonal) and HRP-conjugated streptavidin (1:2000 dilution, catalogue no. N-100, ThermoFisher Scientific). Blots were then visualized using secondary antibodies conjugated with IRDye by an Odyssey imaging system.

### *S*-sulfinylome labeling

Protein *S*-sulfinylome labeling was performed using a diazene-based alkyne probe, DiaAlk[36,37]. Briefly, the cells were treated with 200 μM $H_2O_2$ for 2 hours, washed three times with PBS, and then lysed in modified NP-40 lysis buffer (150 mM NaCl, 0.5% (vol/vol) NP-40, 1 mM EDTA, 1 mM EGTA, 10% (vol/vol) glycerol, and 50 mM Tris, pH 7.4) containing 200 U/mL catalase and protease/phosphatase inhibitors. After 20 min of incubation on ice with frequent mixing, the lysates were clarified by centrifugation at 15,000 *g* at 4 °C for 20 min. The protein lysates were then incubated with 2.5 mM 4,4′-dipyridyldisulfide at room temperature for 1 hour to block free thiols and then filtered through a Micro Bio-Spin P-30 column pre-equilibrated with PBS. The dipyridyldisulfide-free lysates then reacted with 5 mM DiaAlk probe in the dark at room temperature with rotation for 2 hours. Probe-labeled protein samples were added to washed and resuspended streptavidin beads and incubated at 4 °C for 30 min to pre-clean endogenous biotinylated proteins (with 10 μL of streptavidin beads to pre-clean ~100 μg of cell lysates). Protein concentration of the pre-cleaned supernatant was determined using the Pierce BCA protein assay kit and adjusted to a concentration of 2 mg/mL. Click chemistry was then performed by adding 200 μM $N_3$-photo-biotin tag, 1 mM sodium ascorbate, 100 μM Tris[(1-benzyl-1H-1,2,3-triazol-4-yl) methyl] amine (TBTA) ligand, and 1 mM $CuSO_4$. The reaction was allowed to proceed at room temperature for 2 hours before quenching with non-reducing loading buffer. The quenched samples were separated by 12% SDS-PAGE. The *S*-sulfinylome modifications were detected by streptavidin-horseradish peroxidase immunoblotting and CBB R-250 staining served as the loading control.

### ABPP for analyzing cysteine redox states of the mitochondrial proteome

**Isotopic tandem orthogonal proteolysis–ABPP (isoTOP-ABPP).** In situ isoTOP-ABPP labeling of the mitochondrial proteome was performed and modified according to previously reported[29,30]. Briefly, the mitochondria freshly isolated from mouse tissues were quantified using the Pierce BCA protein assay kit and diluted to 2 mg/mL with PBS. Each sample was treated with 100 μM electrophilic iodoacetamide probe (IAyne) at room temperature for 1 hour. After sonication, the click chemistry was initiated by adding 100 μM $N_3$-acid-biotin tag, 1 mM tris (2-carboxyethyl) phosphine, 100 μM TBTA ligand, and 1 mM $CuSO_4$. After incubation at room temperature for 1 hour, the labeled samples were collected by centrifugation (20,000 *g*, 10 min, 4 °C), washed three times with cold methanol, and resuspended in 1.2% SDS/PBS. Samples were diluted to 0.2% SDS/PBS and subjected to streptavidin beads for enrichment for 4 hours at room temperature. The beads were then washed with 0.2% SDS/PBS, PBS and distilled deionized water and pelleted by centrifugation at 1400 *g* for 3 min between washes. The washed beads were suspended in 6 M urea/PBS and then reacted with 10 mM DTT at 35 °C for 30 min. Then 20 mM iodoacetamide was added and allowed to react at 35 °C for 30 min. The beads were then pelleted by centrifugation at 1,400 *g* for 3 min and resuspended in 200 μL PBS containing 2 M urea, 1 mM $CaCl_2$ and 10 ng/μL trypsin. The digestion was allowed to proceed overnight at 37 °C and the beads were washed three times with distilled deionized water. The beads were resuspended in 200 μL of 100 mM triethylammonium bicarbonate buffer and subjected to reductive dimethylation labeling. Briefly, 16 μL of 4% light or heavy formaldehyde was added to control or KO samples. At the same time, 16 μL of 0.6 M sodium cyanoborohydride was added. After labeling for 2 hours at room temperature, the labeled peptides were released from the beads by incubating the beads with 2% FA for 1 hour at room temperature with gentle rotation. After centrifugation at 1400 *g* for 3 min, the supernatant was collected and the cleavage process was repeated and the supernatants were combined. In addition, the beads were washed with 50% acetonitrile and water containing 1% FA, and the washes were combined as the cleavage fraction. Samples were speed-vacuum dried and stored at -30 °C until analysis.

Samples were resuspended in 0.1% FA/$H_2O$ and analyzed by a Q Exactive plus Orbitrap mass spectrometer (Thermo Fisher Scientific)

coupled with nano-LC. Under the positive ion mode, full scan mass spectra were acquired over the m/z range of 350 to 1800 with a resolution of 70,000. The top 20 most intense ions were selected for MS2 fragmentation with a resolution of 17,500 using the collision mode of high energy collision dissociation (HCD). Isolation window was set to 2.0 m/z, normalized collision energy was set to 28%, maximum IT was set to 50 ms, and dynamic exclusion was set to 20 s.

LC-MS/MS raw data were analyzed by ProLuCID[70] with static modification of cysteine (+57.0215 Da) and variable oxidation of methionine (+15.9949 Da). The isotopic modifications (+28.0313 and +34.0631 Da for light and heavy labeling, respectively) were set as static modifications on the N-terminus of a peptide and lysines. IAyne modification (+322.23688 Da) on cysteines was set as variable modification. Heavy/light ratios were quantified using the CIMAGE software[71].

**Data-independent acquisition-based ABPP (DIA-ABPP).** For DIA-ABPP, the procedures including in-situ labeling, click chemistry, streptavidin enrichment, and trypsin digestion of the mitochondrial proteome were performed as for isoTOP-ABPP. Then, samples were directly cleaved with 60-min treatments of 2% and 0.1% FA/$H_2O$ (200 µL) at 25 °C, and the eluents from two cleavage cycles were collected and combined. The samples were then washed with 400 µL 0.1% FA/$H_2O$, and the washes were combined with the eluents to form the cleavage fraction. For data-dependent acquisition (DDA) library generation, 4 cleavage samples were combined and separated into 3 fractions using the Preciex Fractionation Column. All samples were dried using a SpeedVac and resuspended in 0.1% FA/$H_2O$ supplemented with iRT peptides (50/1, vol/vol) before LC-MS/MS analysis.

LC-MS/MS was performed on the Orbitrap Exploris 480 mass spectrometer (Thermo Fisher Scientific) coupled with Vanquish Neo LC system. Mobile phase A was 0.1% FA/$H_2O$, and mobile phase B was 0.1% FA, 80 % acetonitrile in $H_2O$. Flow rate was 3 µL/min for loading and 0.3 µL/min for eluting. The LC gradient was as follows: 0 s-1.8 min, 1%-3% B; 1.8–1.9 min, 3–7% B; 1.9–50.7 min, 7–34% B; 50.7–59.1 min; 34–40% B; 59.1–59.2 min, 40–100% B; 59.2–70 min 100% B. Labeled peptide samples were loaded onto a 75 µm fused silica column packed with 25 cm 1.9µ C18 resin. Under the positive ion mode, full scan mass spectra were acquired over the m/z range of 350 to 1800 using the Orbitrap mass analyzer with a mass resolution of 60,000.

For the DDA mode, MS/MS fragmentation was performed in a data-dependent mode, from which the 20 most intense ions were selected for MS/MS analysis with a resolution of 15,000 using the collision mode of HCD. Isolation window was set to 1.6 m/z, normalized collision energy was set to 30%, maximum IT was set to 50 ms and dynamic exclusion was set to 30 s. Raw data collected by DDA mode were processed using pulsar, the built-in search engine of Spectronaut[72]. 57.0215 Da (carbamidomethylation) and 280.18993 Da (for IA alkyne conjugated acid cleavable tag) were set as variable modifications on cysteines. The function of PTM localization was activated and the cutoff of the site confidence score was set to 0.75. The protein Q value cutoff was set to 1. Other parameters were set as default. Peptide groups were equally distributed among 32 windows according to their mass-to-charge ratios. The number and width of the isolation windows were calculated manually.

For the DIA mode, each DIA cycle contained one full scan and the calculated number of DIA scans covered a mass range of 350–1800 Th with an overlap of 1 Th. For the full MS analysis, the resolution was set to 60,000 and the full MS AGC target was 3E6 with an IT of 30 ms. For each DIA window, the resolution was set to 30,000. AGC target value for fragment spectra was set to 1E6 with an auto IT. Normalized CE was set to 30%. The default charge was 3 and the fixed first mass was set to 100 Th. DIA files were further processed using Spectronaut with the corresponding spectral library. The protein Q value cutoff was set to 1. Other parameters were set as default.

### Quantitative proteomics analysis

Tissues were lysed in lysis buffer (1% SDS, 50 mM HEPES, 50 mM NaCl, 1% glycerol, 5 mM DTT, 1× protease inhibitor, 1× benzonase, pH 8.5) by sonication and centrifuged for protein extraction. Protein concentration was quantified using a Bradford kit. 20 µg of protein was used for analysis. Protein samples were treated with 10 mM DTT for 30 min and 25 mM iodoacetamide for 30 min. Proteins were then extracted using single-pot, solid-phase enhanced sample preparation technology, and were resuspended in 100 mM ammonium bicarbonate and digested by trypsin for 16 hours. Digested peptides of each sample were desalted on C18 tips (Thermo Fisher Scientific). For DDA library generation, 4 tissue samples were combined and separated into 10 fractions using a C18 reverse-phase high-performance liquid chromatography. All the samples were dried by a SpeedVac and resuspended in 0.1% FA/$H_2O$ supplemented with iRT peptides (50/1 v/v) before LC-MS/MS analysis.

LC-MS/MS was performed on the Orbitrap Exploris 480 mass spectrometer coupled with Vanquish Neo LC system. Mobile phase A was 0.1% FA in $H_2O$, and mobile phase B was 0.1% FA, 80 % acetonitrile in $H_2O$. Flow rate was 3 µL/min for loading and 0.3 µL/min for eluting. The LC gradient was as follows: 0 s–1.8 min, 1–3% B; 1.8–2 min, 3–5% B; 2–26 min, 5–15% B; 26–47 min; 15–28% B; 47–54.5 min, 28–38% B; 54.5–54.6 min 38–100% B; 54.6–65 min 100% B. Labeled peptide samples were loaded onto a 75 µm fused silica column packed with 25 cm 1.9µ C18 resin. Under the positive ion mode, full scan mass spectra were acquired over the m/z range of 350 to 1,800 using the Orbitrap mass analyzer with a mass resolution of 60,000.

For the DDA mode, MS/MS fragmentation was performed in a data-dependent mode, from which the 20 most intense ions were selected for MS/MS analysis with a resolution of 15,000 using the collision mode of HCD. Isolation window was set to 1.6 m/z, normalized collision energy was set to 30%, maximum IT was set to 50 ms and dynamic exclusion was set to 30 s. Raw data collected by the DDA mode were processed using pulsar, the built-in search engine of Spectronaut. Parameters were set as default. Peptide groups were equally distributed among 32 windows according to their mass-to-charge ratios. The number and width of the isolation windows were calculated manually.

For the DIA mode, each DIA cycle contained one full scan and the calculated number of DIA scans covered a mass range of 350–1800 Th with an overlap of 1 Th. For the full MS analysis, the resolution was set to 60,000 and the full MS AGC target was 3E6 with an IT of 30 ms. For each DIA window, the resolution was set to 30,000. AGC target value for fragment spectra was set to 1E6 with an auto IT. Normalized CE was set to 30%. Default charge was 3 and the fixed first mass was set to 100 Th. DIA files were further processed using Spectronaut with the corresponding spectral library. Parameters were set as default.

### Immunoblotting analysis of IA-alkyne labeled mitochondrial cysteinome

2 mg/mL mitochondria freshly isolated from the indicated mouse tissues were subjected to in situ IA-alkyne probe labeling and click chemistry was initiated by adding 100 µM $N_3$-acid-biotin tag, 1 mM tris (2-carboxyethyl) phosphine, 100 µM TBTA ligand, and 1 mM $CuSO_4$ after sonication. The reaction was allowed to proceed at room temperature for 1 hour and then terminated with non-reducing loading buffer. After boiling to release biotin-conjugated proteins, the IA-alkyne labeled proteins were analyzed by immunoblotting. CBB R-250 staining served as the loading control.

### Mitochondrial NADPH/($NADP^+$ + NADPH) and GSH/(GSH + GSSG) determination

The ratios of mitochondrial NADPH/($NADP^+$ + NADPH) and GSH/(GSH + GSSG) were measured using the commercial kits (catalogue no. ab65349, ab138881, Abcam) according to the manufacturer's instructions.

### Measurement of respiration

Respiration was measured using the Seahorse XF24 Extracellular Flux Analyzer (Seahorse Bioscience, North Billerica, MA, USA), according to the manufacturer's instructions. For mouse heart mitochondria, 5.0 μg of isolated mitochondria suspended in mitochondrial assay solution (210 mM mannitol, 70 mM sucrose, 10 mM $KH_2PO_4$, 5 mM $MgCl_2$, 1 mM EGTA, 0.2% fatty acid-free BSA, and 2 mM HEPES, pH 7.2) were plated in each well of the XF24 plate. Oxygen consumption rate (OCR) was measured by sequential addition of substrates (10 mM glutamate plus 2 mM malate), 250 μM ADP, 4 μM oligomycin, 4 μM FCCP, and 2 μM antimycin A. To measure OCR of hepatocytes, 10 mM glucose and 1 mM pyruvate were used as substrates. 1 μM oligomycin, 1 μM FCCP, and 1 μM rotenone/antimycin A were added sequentially. Basal OCR, ATP production coupled OCR, proton leak OCR, and maximal OCR were obtained. All data were analyzed using the XF24 software.

### Measurement of mitochondrial $Ca^{2+}$ uptake

Isolated mitochondria from the heart or liver were resuspended in the buffer containing 110 mM KCl, 0.5 mM $KH_2PO_4$, 1 mM $MgCl_2$, 0.01 mM EGTA, 5 mM succinate, 2 μM rotenone, and 20 mM HEPES, pH 7.2. 0.2 μM Fluo-5N pentapotassium salt was added to the mitochondrial suspension with gentle stirring and the fluorescence signals were monitored at 490 nm excitation/516 nm emission on a PTI spectrofluorometer (RF-5301PC, SHIMADZU Co.). After 120 seconds of basal recording, a bolus of 20 μM $Ca^{2+}$ was added, and the clearance of extramitochondrial $Ca^{2+}$ reported by the decrease in Fluo-5N fluorescence indicated mitochondrial $Ca^{2+}$ uptake. At 420 seconds, 1 μM Ru360 was added to inhibit mitochondrial $Ca^{2+}$ uptake. At 720 seconds, 1 μM FCCP was added to induce total mitochondrial $Ca^{2+}$ release. 250 μg of heart mitochondria and 500 μg of liver mitochondria were used for each measurement, respectively.

### Confocal microscopy and image processing

A Zeiss LSM710 inverted confocal microscope equipped with a 40×, 1.3NA oil immersion objective was used for acquiring images. All experiments were performed in Tyrode's solution (137 mM NaCl, 5.4 mM KCl, 1.2 mM $NaH_2PO_4$•$2H_2O$, 10 mM D-glucose, 1.2 mM $MgCl_2$•$6H_2O$, 1.8 mM $CaCl_2$, and 20 mM HEPES, pH 7.35) at room temperature.

For mitochondrial membrane potential measurement, isolated cardiomyocytes were loaded with 50–100 nM TMRM at 37 °C for 10 min, followed by three washes. The TMRM fluorescence was imaged with excitation at 543 nm and emission collection at >560 nm. To simultaneously measure mitochondrial $Ca^{2+}$ uptake and cytosolic $Ca^{2+}$ transient, HeLa cells transiently transfected with WT or mutant ROMO1-FLAG were loaded with 5 μM Rhod-2 AM at 37 °C for 30 min and 5 μM Fluo-4 AM at 37 °C for 10 min followed by three washes with Tyrode's solution before imaging. Mitochondrial and cytosolic $Ca^{2+}$ dynamics were recorded before and after 100 μM histamine stimulation. Fluorescence of Rhod-2 and Fluo-4 was imaged with excitation at 561 nm and 488 nm and emission collected at 580-740 nm and at >500 nm, respectively. Confocal images were analyzed using Zen 2010 (Zeiss) and custom programs.

### Echocardiography

Transthoracic echocardiography was performed using a Vevo2100 or Vevo3100 system equipped with an MS400 transducer (VisualSonics, Toronto, ON). Mice were anesthetized with isoflurane (3–5% in 100% $O_2$ at 0.5 L/min), and deep anesthesia was confirmed by lack of response to firm pressure on the hind paws. During echocardiogram acquisition, the dose of isoflurane was reduced to 0.5-1.0% to maintain a relatively stable heart rate at about 500 beats per minute with real-time body temperature and electrocardiographic monitoring. The heart was imaged using M-mode, and two-dimensional measurements were made at the position of the papillary muscles. Parameters collected included heart rate, left ventricular end-diastolic and end-systolic diameters, and left ventricular anterior and posterior wall thicknesses in the end-diastolic and end-systolic phases. Left ventricular ejection fraction and left ventricular fractional shortening were used to assess systolic function. Data represent the average of at least five separate scans in a random-blind fashion.

### Grip strength test

Grip strength of fore and hind limbs was assessed using a grip strength meter (Chatillon Force Measurement Systems, Largo, FL). Mice were lifted by their tails and allowed to grasp the steel grid attached to the apparatus with their forepaws and backpaws. The mouse was then gently pulled across the steel grid until its grip was released. Each mouse was tested 5 times and the three highest measurements were averaged to calculate grip strength.

### Cross-sectional area analysis of muscle fiber

Excised gastrocnemius tissues were fixed with 4% paraformaldehyde and embedded in paraffin. Tissue samples were cut at a thickness of 6 μm and the sections were stained with hematoxylin eosin. The mean cross-sectional area of the fibers was determined using the Image J.

### Plasma parameter analysis

Blood was collected using heparinized tubes from the inferior vena cava immediately after sacrifice of the mice, then transferred to 1.5 mL tubes and centrifuged at 2000 *g* for 15 min at 4 °C. The supernatant after centrifugation was used for analysis of AST, ALT, LDL, HDL, cholesterol, and triglyceride using a fully automated Roche Cobas c311 platform (Roche Holding, Basel, Switzerland). Interleukin-6 level was measured with an ELISA kit (catalogue no. D721022, Sangong Biotech).

### Bioinformatic analysis

Mitochondrial protein sub-localization was annotated referring to MitoCarta (v3.0)[19]. Disease-gene association analyses were based on the DisGeNET database. Functional annotation and pathway enrichment analyses were performed using the Database for Annotation, Visualization, and Integrated Discovery with a P-value cutoff of 0.05 under the Benjamini test[73,74].

### Statistical analysis

Data are presented as mean ± s.e.m. or mean ± s.d. of multiple biological replicates or independent experiments as indicated. Statistical analysis was performed using GraphPad Prism v9.0.0 software or Microsoft Excel. Two-tailed unpaired Student's *t*-test with Welch's correction or two-way ANOVA with Tukey's multiple comparison test was applied to determine statistical significance. $P < 0.05$ was considered statistically significant.

### Reporting summary

Further information on research design is available in the Nature Portfolio Reporting Summary linked to this article.

## Data availability

Proteomics raw data and Spectronaut search tables are available via ProteomeXchange (http://proteomecentral.proteomexchange.org) under identifier PXD052999. MS raw data of intermolecular disulfide bonds are available under identifier PXD053027. Source data are provided with this paper.

## Code availability

We did not generate any custom code and utilized software packages with prewritten code and default parameters for analysis of mass spectrometry and imaging data in this study.

## References


1. Winterbourn, C. C. & Hampton, M. B. Thiol chemistry and specificity in redox signaling. *Free Radic. Biol. Med* **45**, 549–561 (2008).
2. Go, Y. M., Chandler, J. D. & Jones, D. P. The cysteine proteome. *Free Radic. Bio Med* **84**, 227–245 (2015).
3. Holmstrom, K. M. & Finkel, T. Cellular mechanisms and physiological consequences of redox-dependent signalling. *Nat. Rev. Mol. Cell Biol.* **15**, 411–421 (2014).
4. Paulsen, C. E. & Carroll, K. S. Cysteine-mediated redox signaling: chemistry, biology, and tools for discovery. *Chem. Rev.* **113**, 4633–4679 (2013).
5. Bak, D. W. & Weerapana, E. Cysteine-mediated redox signalling in the mitochondria. *Mol. Biosyst.* **11**, 678–697 (2015).
6. Murray, C. I. & Van Eyk, J. E. Chasing cysteine oxidative modifications: proteomic tools for characterizing cysteine redox status. *Circ. Cardiovasc Genet* **5**, 591 (2012).
7. Go, Y. M., Duong, D. M., Peng, J. & Jones, D. P. Protein cysteines map to functional networks according to steady-state level of oxidation. *J. Proteom. Bioinform* **4**, 196–209 (2011).
8. Hansen, R. E., Roth, D. & Winther, J. R. Quantifying the global cellular thiol-disulfide status. *P Natl Acad. Sci. USA* **106**, 422–427 (2009).
9. Requejo, R., Hurd, T. R., Costa, N. J. & Murphy, M. P. Cysteine residues exposed on protein surfaces are the dominant intramitochondrial thiol and may protect against oxidative damage. *Febs J.* **277**, 1465–1480 (2010).
10. Fra, A., Yoboue, E. D. & Sitia, R. Cysteines as redox molecular switches and targets of disease. *Front Mol. Neurosci.* **10**, 167 (2017).
11. Schieber, M. & Chandel, N. S. ROS function in redox signaling and oxidative stress. *Curr. Biol.* **24**, R453–R462 (2014).
12. Zorov, D. B., Juhaszova, M. & Sollott, S. J. Mitochondrial reactive oxygen species (ROS) and ROS-induced ROS release. *Physiol. Rev.* **94**, 909–950 (2014).
13. Bulaj, G., Kortemme, T. & Goldenberg, D. P. Ionization-reactivity relationships for cysteine thiols in polypeptides. *Biochemistry* **37**, 8965–8972 (1998).
14. Mailloux, R. J., Jin, X. & Willmore, W. G. Redox regulation of mitochondrial function with emphasis on cysteine oxidation reactions. *Redox Biol.* **2**, 123–139 (2014).
15. Han, D. et al. Sites and mechanisms of aconitase inactivation by peroxynitrite: Modulation by citrate and glutathione. *Biochemistry* **44**, 11986–11996 (2005).
16. Chouchani, E. T. et al. Cardioprotection by S-nitrosation of a cysteine switch on mitochondrial complex I. *Nat. Med* **19**, 753–759 (2013).
17. Riemer, J., Schwarzlander, M., Conrad, M. & Herrmann, J. M. Thiol switches in mitochondria: operation and physiological relevance. *Biol. Chem.* **396**, 465–482 (2015).
18. Go, Y. M. & Jones, D. P. Thiol/disulfide redox states in signaling and sensing. *Crit. Rev. Biochem Mol. Biol.* **48**, 173–181 (2013).
19. Rath, S. et al. MitoCarta3.0: an updated mitochondrial proteome now with sub-organelle localization and pathway annotations. *Nucleic Acids Res.* **49**, D1541–D1547 (2021).
20. Morgenstern, M. et al. Quantitative high-confidence human mitochondrial proteome and its dynamics in cellular context. *Cell Metab.* **33**, 2464–2483 e2418 (2021).
21. Chung, Y. M., Kim, J. S. & Yoo, Y. D. A novel protein, Romo1, induces ROS production in the mitochondria. *Biochem Biophys. Res. Commun.* **347**, 649–655 (2006).
22. Chung, J. S. et al. Mitochondrial reactive oxygen species originating from Romo1 exert an important role in normal cell cycle progression by regulating p27(Kip1) expression. *Free Radic. Res.* **43**, 729–737 (2009).
23. Chung, J. S. et al. Overexpression of Romo1 promotes production of reactive oxygen species and invasiveness of hepatic tumor cells. *Gastroenterology* **143**, 1084–1094 e1087 (2012).
24. Chung, Y. M. et al. Replicative senescence induced by Romo1-derived reactive oxygen species. *J. Biol. Chem.* **283**, 33763–33771 (2008).
25. Na, A. R. et al. A critical role for Romo1-derived ROS in cell proliferation. *Biochem Biophys. Res Commun.* **369**, 672–678 (2008).
26. Shin, J. A., Chung, J. S., Cho, S. H., Kim, H. J. & Yoo, Y. D. Romo1 expression contributes to oxidative stress-induced death of lung epithelial cells. *Biochem Biophys. Res Commun.* **439**, 315–320 (2013).
27. Richter, F. et al. ROMO1 is a constituent of the human presequence translocase required for YME1L protease import. *J. Cell Biol.* **218**, 598–614 (2019).
28. Norton, M. et al. ROMO1 is an essential redox-dependent regulator of mitochondrial dynamics. *Sci. Signal* **7**, ra10 (2014).
29. Weerapana, E. et al. Quantitative reactivity profiling predicts functional cysteines in proteomes. *Nature* **468**, 790–795 (2010).
30. Yang, F., Gao, J., Che, J., Jia, G. & Wang, C. A dimethyl-labeling-based strategy for site-specifically quantitative chemical proteomics. *Anal. Chem.* **90**, 9576–9582 (2018).
31. Lam, S. S. et al. Directed evolution of APEX2 for electron microscopy and proximity labeling. *Nat. Methods* **12**, 51–54 (2015).
32. Jumper, J. et al. Highly accurate protein structure prediction with AlphaFold. *Nature* **596**, 583–589 (2021).
33. Varadi, M. et al. AlphaFold Protein Structure Database: massively expanding the structural coverage of protein-sequence space with high-accuracy models. *Nucleic Acids Res* **50**, D439–D444 (2022).
34. Nicholls, D. G. & Ferguson, S. L. *Bioenergetics*, (Academic Press, 2002).
35. Bota, D. A. & Davies, K. J. Lon protease preferentially degrades oxidized mitochondrial aconitase by an ATP-stimulated mechanism. *Nat. Cell Biol.* **4**, 674–680 (2002).
36. Akter, S. et al. Chemical proteomics reveals new targets of cysteine sulfinic acid reductase. *Nat. Chem. Biol.* **14**, 995–1004 (2018).
37. Meng, J. et al. Global profiling of distinct cysteine redox forms reveals wide-ranging redox regulation in C. elegans. *Nat. Commun.* **12**, 1415 (2021).
38. Bernardi, P., Rasola, A., Forte, M. & Lippe, G. The mitochondrial permeability transition pore: channel formation by F-ATP synthase, integration in signal transduction, and role in pathophysiology. *Physiol. Rev.* **95**, 1111–1155 (2015).
39. Morciano, G. et al. The mitochondrial permeability transition pore: an evolving concept critical for cell life and death. *Biol. Rev. Camb. Philos. Soc.* **96**, 2489–2521 (2021).
40. Carraro, M., Carrer, A., Urbani, A. & Bernardi, P. Molecular nature and regulation of the mitochondrial permeability transition pore(s), drug target(s) in cardioprotection. *J. Mol. Cell Cardiol.* **144**, 76–86 (2020).
41. Karch, J. et al. Inhibition of mitochondrial permeability transition by deletion of the ANT family and CypD. *Sci. Adv.* **5**, eaaw4597 (2019).
42. Kokoszka, J. E. et al. The ADP/ATP translocator is not essential for the mitochondrial permeability transition pore. *Nature* **427**, 461–465 (2004).
43. Baines, C. P. et al. Loss of cyclophilin D reveals a critical role for mitochondrial permeability transition in cell death. *Nature* **434**, 658–662 (2005).
44. Basso, E. et al. Properties of the permeability transition pore in mitochondria devoid of Cyclophilin D. *J. Biol. Chem.* **280**, 18558–18561 (2005).
45. Nakagawa, T. et al. Cyclophilin D-dependent mitochondrial permeability transition regulates some necrotic but not apoptotic cell death. *Nature* **434**, 652–658 (2005).
46. Schinzel, A. C. et al. Cyclophilin D is a component of mitochondrial permeability transition and mediates neuronal cell death after focal cerebral ischemia. *Proc. Natl Acad. Sci. USA* **102**, 12005–12010 (2005).

47. Giorgio, V. et al. Dimers of mitochondrial ATP synthase form the permeability transition pore. *Proc. Natl Acad. Sci. USA* **110**, 5887–5892 (2013).
48. Alavian, K. N. et al. An uncoupling channel within the c-subunit ring of the F1FO ATP synthase is the mitochondrial permeability transition pore. *Proc. Natl Acad. Sci. USA* **111**, 10580–10585 (2014).
49. Baughman, J. M. et al. Integrative genomics identifies MCU as an essential component of the mitochondrial calcium uniporter. *Nature* **476**, 341–345 (2011).
50. De Stefani, D., Raffaello, A., Teardo, E., Szabo, I. & Rizzuto, R. A forty-kilodalton protein of the inner membrane is the mitochondrial calcium uniporter. *Nature* **476**, 336–340 (2011).
51. Balaban, R. S., Nemoto, S. & Finkel, T. Mitochondria, oxidants, and aging. *Cell* **120**, 483–495 (2005).
52. Harrington, J. S., Ryter, S. W., Plataki, M., Price, D. R. & Choi, A. M. K. Mitochondria in health, disease, and ageing. *Physiol. Rev.* **103**, 2349–2422 (2023).
53. Demontis, F., Piccirillo, R., Goldberg, A. L. & Perrimon, N. Mechanisms of skeletal muscle aging: insights from Drosophila and mammalian models. *Dis. Model Mech.* **6**, 1339–1352 (2013).
54. Droge, W. Free radicals in the physiological control of cell function. *Physiol. Rev.* **82**, 47–95 (2002).
55. Lopez-Otin, C., Blasco, M. A., Partridge, L., Serrano, M. & Kroemer, G. Hallmarks of aging: An expanding universe. *Cell* **186**, 243–278 (2023).
56. Salmon, A. B., Richardson, A. & Perez, V. I. Update on the oxidative stress theory of aging: does oxidative stress play a role in aging or healthy aging?. *Free Radic. Biol. Med* **48**, 642–655 (2010).
57. Murphy, M. P. How mitochondria produce reactive oxygen species. *Biochem J.* **417**, 1–13 (2009).
58. Perez, M. J. & Quintanilla, R. A. Development or disease: duality of the mitochondrial permeability transition pore. *Dev. Biol.* **426**, 1–7 (2017).
59. Xiao, H. P. et al. A quantitative tissue-specific landscape of protein redox regulation during aging. *Cell* **180**, 968–983 (2020).
60. Zheng, M. et al. Cardiac-specific ablation of Cypher leads to a severe form of dilated cardiomyopathy with premature death. *Hum. Mol. Genet* **18**, 701–713 (2009).
61. Henderson, S. A. et al. Structure, organization, and expression of the rat cardiac myosin light chain-2 gene. Identification of a 250-base pair fragment which confers cardiac-specific expression. *J. Biol. Chem.* **264**, 18142–18148 (1989).
62. Huber, I. et al. Identification and selection of cardiomyocytes during human embryonic stem cell differentiation. *FASEB J.* **21**, 2551–2563 (2007).
63. Tani, Y. et al. Molecular cloning of the rat thyroxine-binding globulin gene and analysis of its promoter activity. *Endocrinology* **135**, 2731–2736 (1994).
64. Cotugno, G. et al. Impact of age at administration, lysosomal storage, and transgene regulatory elements on AAV2/8-mediated rat liver transduction. *PLoS One* **7**, e33286 (2012).
65. Hou, T. et al. NDUFAB1 confers cardio-protection by enhancing mitochondrial bioenergetics through coordination of respiratory complex and supercomplex assembly. *Cell Res* **29**, 754–766 (2019).
66. Plugis, N. M. et al. Interleukin 4 is inactivated via selective disulfide-bond reduction by extracellular thioredoxin. *P Natl Acad. Sci. USA* **115**, 8781–8786 (2018).
67. Jin, X. et al. Activation of Extracellular Transglutaminase 2 by Thioredoxin. *J. Biol. Chem.* **286**, 37866–37873 (2011).
68. Brandstaedter, C. et al. Kinetic characterization of wild-type and mutant human thioredoxin glutathione reductase defines its reaction and regulatory mechanisms. *Febs J.* **285**, 542–558 (2018).
69. Lambert, N. & Freedman, R. B. Kinetics and specificity of homogeneous protein disulfide-isomerase in protein disulfide isomerization and in thiol protein-disulfide oxidoreduction. *Biochem J.* **213**, 235–243 (1983).
70. Xu, T. et al. ProLuCID: An improved SEQUEST-like algorithm with enhanced sensitivity and specificity. *J. Proteom.* **129**, 16–24 (2015).
71. Gao, J. et al. CIMAGE2.0: an expanded tool for quantitative analysis of activity-based protein profiling (ABPP) data. *J. Proteome Res* **20**, 4893–4900 (2021).
72. Bruderer, R. et al. Extending the limits of quantitative proteome profiling with data-independent acquisition and application to acetaminophen-treated three-dimensional liver microtissues. *Mol. Cell Proteom.* **14**, 1400–1410 (2015).
73. Huang da, W., Sherman, B. T. & Lempicki, R. A. Bioinformatics enrichment tools: paths toward the comprehensive functional analysis of large gene lists. *Nucleic Acids Res* **37**, 1–13 (2009).
74. Huang da, W., Sherman, B. T. & Lempicki, R. A. Systematic and integrative analysis of large gene lists using DAVID bioinformatics resources. *Nat. Protoc.* **4**, 44–57 (2009).


## Acknowledgements

We thank Dr. Song Yao for technical support in echocardiography, Dr. Hongri Gong for providing the SDH complex, and Drs. Ruiping Xiao, Xinli Hu, Xi Wang, and Lei Wang for valuable comments. This work was supported by the Shenzhen Medical Research Fund (B2402022), the National Natural Science Foundation of China (32293210, 32470732 and 92157105), the National Science and Technology Innovation 2030 Major Program (2022ZD0211900), the National Key Basic Research Program of China (2017YFA0504000), and CAMS Innovation Fund for Medical Sciences (2019-I2M-5-054).

## Author contributions

X.W. and H.C. conceived and supervised the study. F.X. designed and performed most experiments and was involved in all aspects of this study; H.H. designed and performed the experiments related to aging study; C.J. and Y.W. assisted the generation of TG and cKO mouse models; H.W. performed APEX proximity labeling; K.P. and S.Q. performed aconitase activity assays; Y.C. assisted in isoTOP-ABPP experiments and analysis under the supervision of C.W.; K.L. and L.F. assisted in S-sulfinylome labeling assay and intermolecular disulfide identification under the supervision of J.Y.; Z.J. and X.D. assisted in proteomics analysis; X.W., F.X., and H.C. wrote the manuscript. All authors participated in the discussion and data interpretation and critically reviewed and approved the final version of the manuscript.

## Competing interests

The authors declare no competing interests.

## Additional information

**Supplementary information** The online version contains supplementary material available at https://doi.org/10.1038/s41467-025-60503-z.

**Correspondence** and requests for materials should be addressed to Heping Cheng or Xianhua Wang.

**Peer review information** *Nature Communications* thanks the anonymous reviewer(s) for their contribution to the peer review of this work. A peer review file is available.